

RESPONSE TO QUESTIONS 6, 8, 9, 15
17, 18, and 19

October 1989

This volume responds to the remaining 7 of 19 questions asked of PG&E by the Nuclear Regulatory Commission (NRC) on June 1, 1989. These responses provide data requested to augment or clarify information regarding seismic ground motions presented in the Final Report of the Long Term Seismic Program, submitted by PG&E to the NRC on July 31, 1988, and in the responses to Questions 4 through 18 and 20, submitted by PG&E to the NRC in January and February 1989.

8911010063 891019
PDR ADCK 05000275
P PNU



Pacific Gas and Electric Company

Diablo Canyon Power Plant
Long Term Seismic Program



QUESTION 6

Is the apparent magnitude dependence of the dispersion in the empirical ground-motion analysis real or is it an artifact of the data set? For lower magnitudes the uncertainty may be due to inter-event dispersion while at larger magnitudes it may be due to intra-event dispersion.

Introduction

The relationships for dispersion in ground-motion parameters given in the Final Report (Table 4-5, p. 4-38) were based on analyses of the ground-motion data base assembled for the project, and on the results of studies published by Idriss and others (1982), Sadigh (1983), and Sadigh and others (1986). The dispersion values listed in Table 4-5 for earthquakes of magnitude 6.5 and greater were based on detailed analyses of ground-motion data recorded on rock from large-magnitude earthquakes. The dispersion relationships were extended to smaller magnitudes using the published results cited above. These studies indicate that dispersion in peak ground-motion parameters is strongly dependent on earthquake magnitude.

Figure Q6-1 presents a typical result from the cited studies. The magnitude dependence in dispersion was evaluated by computing the standard error in the natural logarithm of a peak ground-motion parameter for data from narrow magnitude bands. The ground-motion data base used in those studies consisted primarily of recordings from two earthquakes: San Fernando, 1971 (6.6 M_w), and Imperial Valley, 1979 (6.5 M_w), and recordings from a large number of magnitude 4 to 6 aftershocks from three earthquakes sequences, Oroville, 1975, Imperial Valley, 1979, and Mammoth Lakes, 1980.

There are large differences in the number of earthquakes represented in the ground-motion data base at large and at small magnitudes. The Long Term Seismic Program data base contains recordings from 13 earthquakes of magnitude 6.3 and greater, and from more than 40 earthquakes in the magnitude range of 4 to 5. If the dispersion in ground-motion is modeled as consisting of intra-event dispersion and inter-event dispersion, as was done by Joyner and Boore (1981), then the total dispersion for large-magnitude earthquakes may be less reliably estimated due to the smaller number of events in the data base. It should be noted, however, that the smaller number of events does not mean that the dispersion for large-magnitude events is necessarily underestimated, only that the inter-event component of total dispersion may be less reliably estimated than for the smaller magnitude events.

To respond to the question, a large data base of soil- and rock-site peak acceleration values was compiled. These data were first examined in the conventional manner to identify trends in the dispersion. The data were then analyzed using a formal model that treats the variance in logarithm of peak ground acceleration as consisting of an inter-event and an intra-event component. The dependence of each variance component on earthquake magnitude was investigated. Additional evidence that the intra-event component is magnitude dependent was provided by the study by Abrahamson (1988). This study showed that the standard error in the logarithmic value of peak acceleration recorded for individual events by the SMART 1 array in Taiwan decreased as the magnitude of the event increased (Figure Q6-2). Our review of the literature and rigorous statistical analysis of a large strong motion data set indicate that the apparent magnitude dependence of the dispersion in the empirical ground-motion analysis is a statistically significant characteristic of strong ground motion, and is not an artifact of the data.

Strong Motion Data Base

The ground-motion data analyzed in response to this question consisted of the data base used to develop the relationships presented in the Final Report augmented by more recent recordings, data from smaller magnitude earthquakes, and data from soil-site recordings. Combining rock- and soil-site data increases the number of recordings and results in more stable estimates of dispersion,





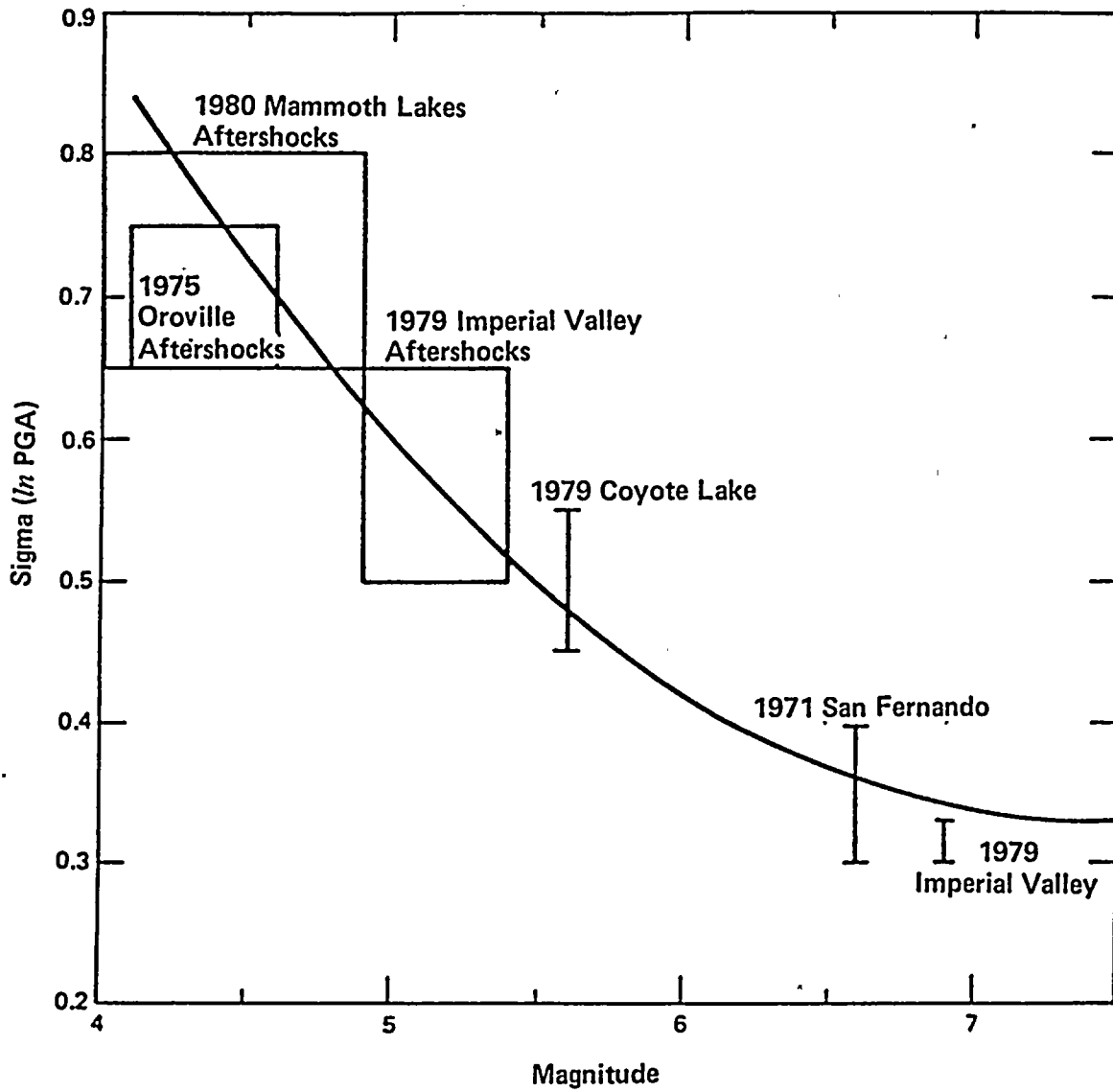


Figure Q6-1

Variation of dispersion for peak ground acceleration as a function of magnitude (modified from Sadigh, 1983).



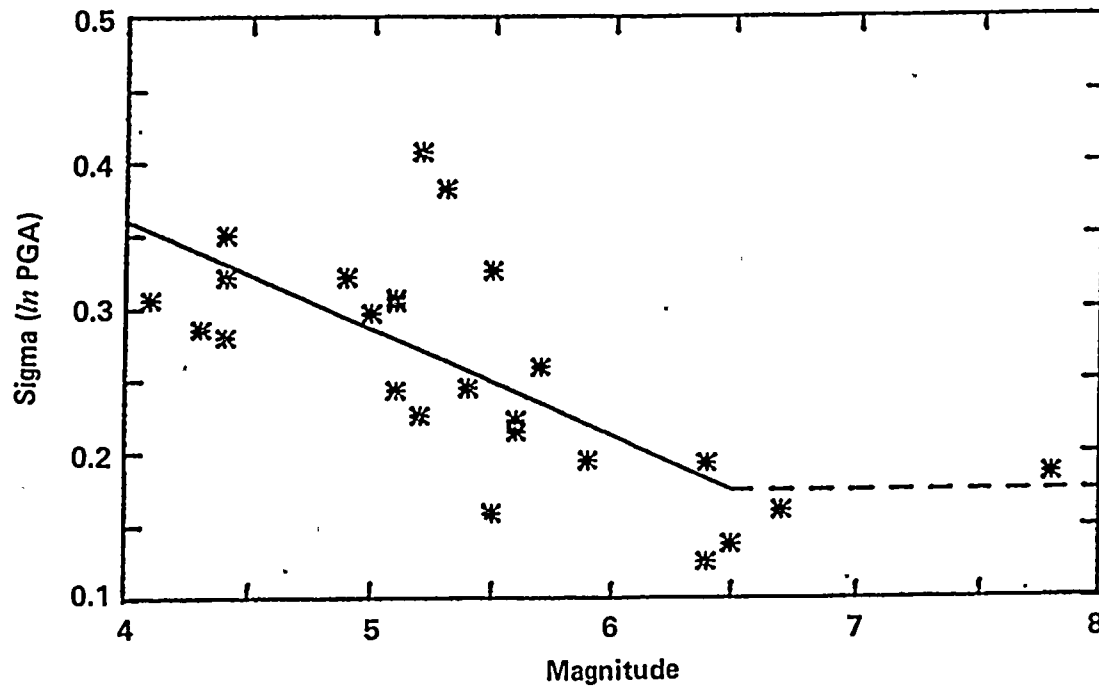


Figure Q6-2

Magnitude dependence of the intra-event dispersion from earthquakes recorded by the SMART 1 array in Taiwan (from Abrahamson, 1988).





especially for events of magnitudes less than 5, where there is very limited rock-site data. The combined data base consists of 803 recordings from 124 earthquakes having moment magnitudes between 3.8 and 7.4, and source-to-site distances less than 100 km. Figure Q6-3 shows the distribution of the data in terms of magnitude, distance, and peak acceleration.

A multiple regression analysis was made on the combined data set using the functional form of the median attenuation relationship employed in the Long Term Seismic Program Final Report, that is

$$\ln(a_{\max}) = C_1 + C_2M + C_3 \ln(R + C_4 \exp(C_5M)) + C_6Z_f \quad (1)$$

where a_{\max} is the geometric average of the two peak horizontal components of acceleration, M is moment magnitude, R is source-to-site distance, C_1 through C_6 are coefficients estimated from the data, and Z_f is a style of faulting index equal to 0 for strike-slip faulting and equal to 1 for reverse faulting. Assuming homoscedasticity (constant variance for all values of the independent variables M , R , and Z_f), the fitted relationship has a standard error of 0.604. No differentiation was made between soil- and rock-site data in the analysis, because the effect of local site type cannot be adequately modeled by a simple constant. Figure Q6-4 shows the normalized residuals resulting from the fit of Equation (1) to the data. The soil dispersion and rock dispersion values are similar: 0.64 for rock and 0.60 for soil. Therefore, for estimating magnitude-dependent dispersion, the soil- and rock-site data can be combined.

As indicated by the results shown in Figure Q6-4, the dispersion of the logarithm of peak acceleration decreases as earthquake magnitude increases. When the data are divided into three magnitude bands having an approximately equal number of records represented in each band, the resulting standard errors are as follows:

<u>Magnitude Band</u>	<u>Number of Records</u>	<u>Number of Earthquakes</u>	<u>Mean Magnitude</u>	<u>Standard Error</u>
3.8 to 5.2	269	78	4.5	0.700
5.3 to 6.1	269	32	5.7	0.606
6.2 to 7.4	265	14	6.4	0.496

When the data are divided into three magnitude bands having an approximately equal number of earthquakes represented in each band, the resulting standard errors are as follows:

<u>Magnitude Band</u>	<u>Number of Earthquakes</u>	<u>Number of Records</u>	<u>Mean Magnitude</u>	<u>Standard Error</u>
3.8 to 4.4	40	120	4.0	0.745
4.5 to 5.3	44	203	5.0	0.668
5.4 to 7.4	40	480	6.1	0.530

The differences in standard errors between the various magnitude bands are large enough to reject the hypothesis that the variance is constant at less than the 5-percent level in most cases, and at less than the 1-percent level for the largest magnitude band. The second set of results given above clearly shows the effect of magnitude on dispersion when considering data groups representing large numbers of earthquakes. These results were analyzed in a more rigorous manner, as discussed below.

Analysis of Variance Components of Strong Ground-motion

The variance components of peak ground-motion were analyzed using a random effects model. This model was used by Brillinger and Preisler (1984, 1985) to analyze Joyner and Boore's (1981) data set. They obtained almost the same attenuation model as Joyner and Boore (1981) under the assumption that peak ground acceleration is lognormally distributed.



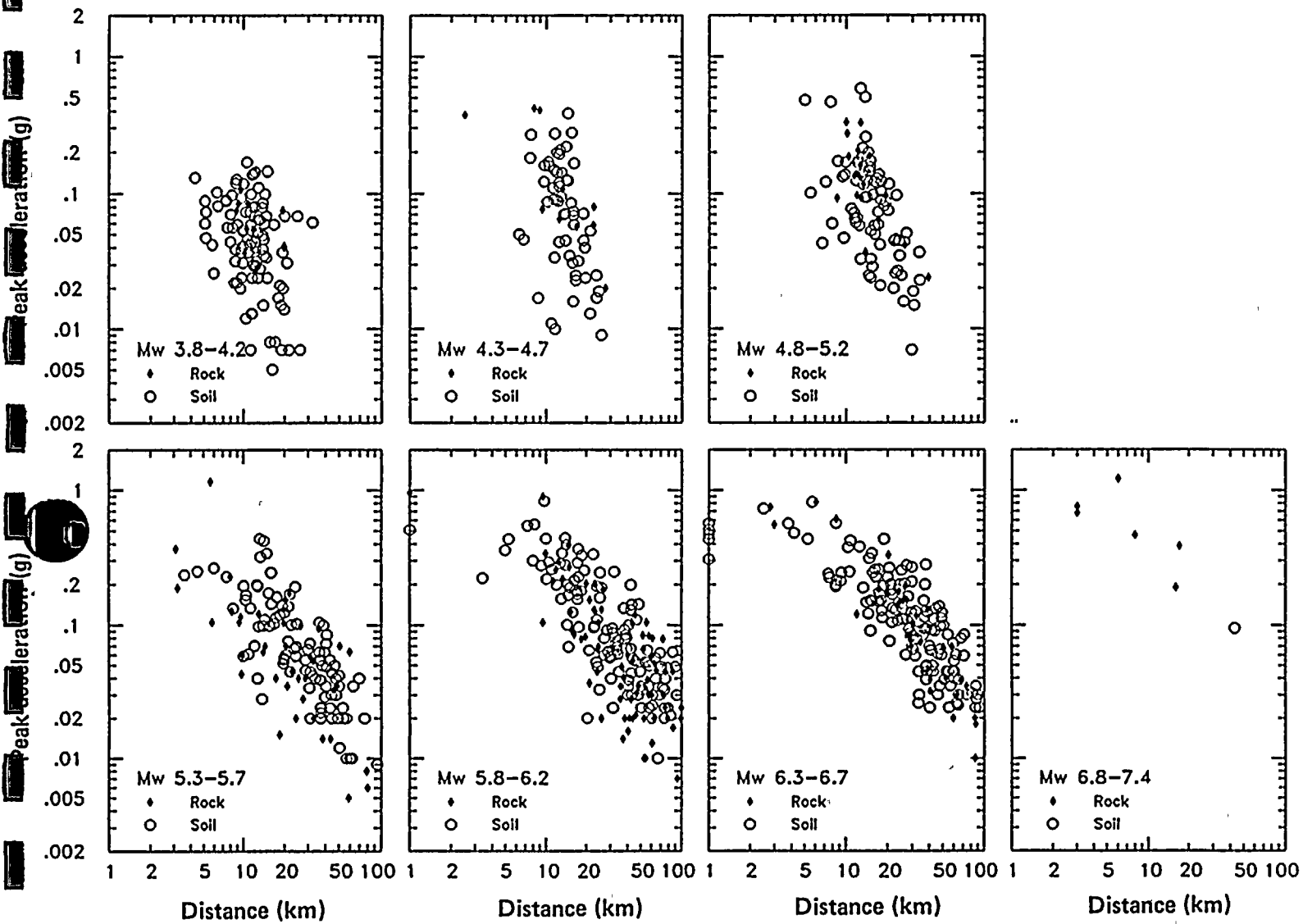


Figure Q6-3

Strong-motion data set used in variance analysis.



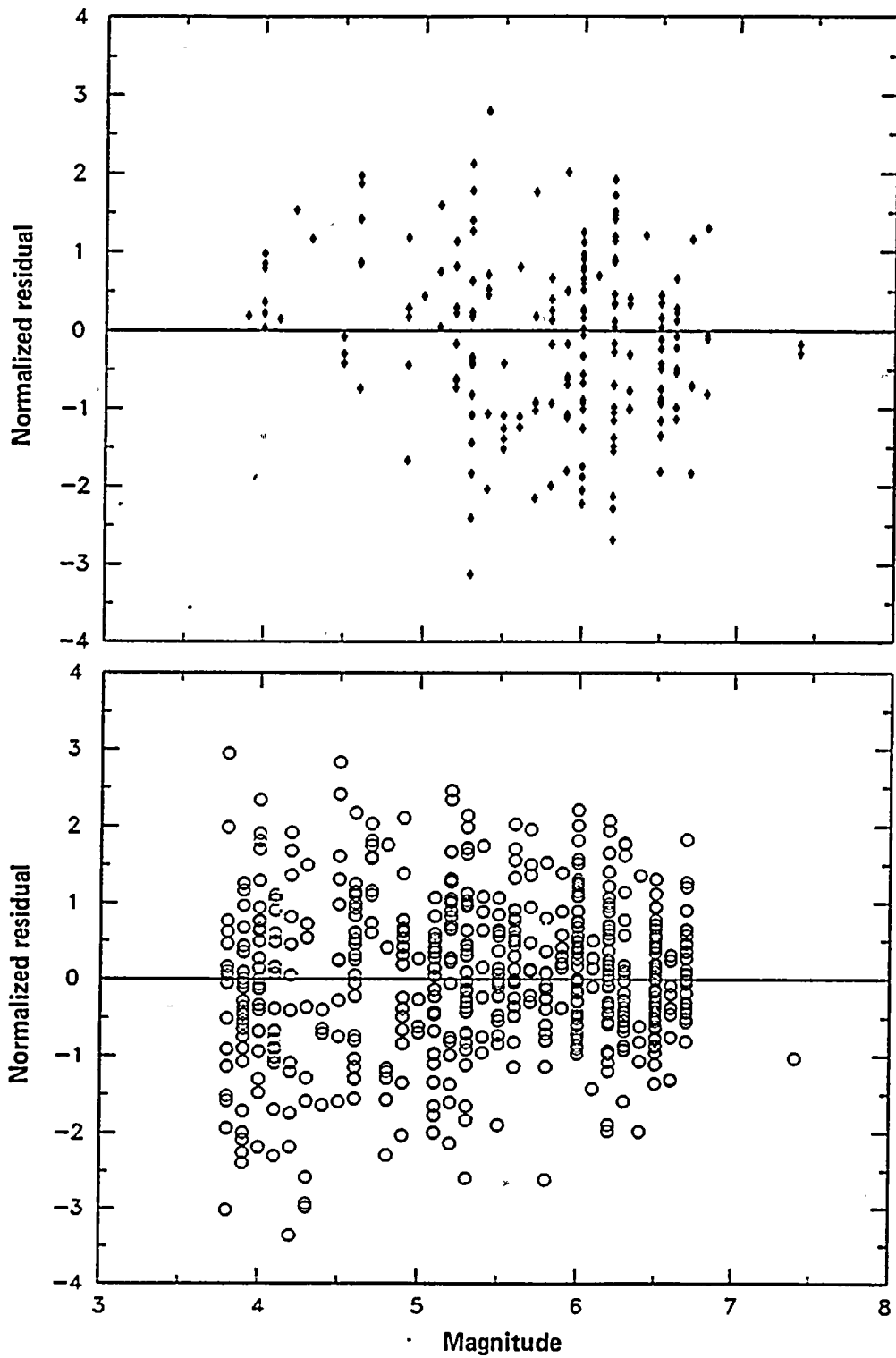


Figure Q6-4

Normalized residuals from fit of Equation (2) to data shown in Figure Q6-3.





The usual approach for deriving empirical ground-motion attenuation relationships is to perform regressions using the model

$$\ln(a_{ij}) = f(M_i, R_j, Z_{fj}, \Theta) + \epsilon_{ij} \quad (2)$$

where a_{ij} is the peak ground-motion at the j^{th} site from the i^{th} earthquake, Θ is a vector of model parameters (C_1 through C_6 in Equation 1), and ϵ_{ij} is the error term, considered to be probabilistically independent from site to site and from event to event, with variance σ^2 , which is functionally independent of M , R , and Z_{fj} , or, homoscedastic. This type of model is termed a fixed effects model.

The random effects model, as employed by Brillinger and Preisler (1984, 1985) partitions the error term into inter-event and intra-event terms. They used a model of the form

$$\ln(a_{ij}) = f(M_i, R_j, Z_{fj}, \Theta) + \epsilon_i + \epsilon_{ij} \quad (3)$$

where ϵ_i represents a random effect common to all recordings of the i^{th} event. The ϵ_i and ϵ_{ij} are assumed to be independent of each other and normally distributed, with variances τ^2 and σ^2 , respectively. The total variance in peak ground-motion is equal to the sum of the two parts, $\sigma_T^2 = \tau^2 + \sigma^2$. This type of model allows a direct evaluation of the inter-event and intra-event contributions to dispersion at small and large magnitudes.

If the data base contains a large number of recordings of each earthquake, then inter-event dispersion can be estimated directly; the estimate of ϵ_i is given by the mean residual for the i^{th} event. The variances τ^2 and σ^2 can then be estimated directly from the ϵ_i and the intra-event residuals ($\ln(a_{ij}) - [f(M_i, R_j, Z_{fj}, \Theta) + \epsilon_i]$), respectively. Generally, however, the data base is not complete, with many events having only a few recordings. In particular, if there is only one recording from an event, then a direct estimate of ϵ_i can not be made. To avoid such difficulties, the maximum likelihood method was used to estimate the variance components. This is the most common method employed to evaluate random effects models.

The likelihood formulation for mixed models, containing both random and fixed effects, has several published references (for example, Searle, 1971). Assuming normality, the log-likelihood function, L , is given by

$$L = -\frac{1}{2} \ln |V| - \frac{1}{2} [y - f(M, R, Z_f, \Theta)]^T V^{-1} [y - f(M, R, Z_f, \Theta)] \quad (4)$$

where y is the vector of observed values of $\ln(a_{ij})$, $f(M, R, Z_f, \Theta)$ is the vector of predicted responses from the fixed effects, and V is the covariance matrix of y containing both error terms ϵ_i and ϵ_{ij} .

Brillinger and Preisler (1985) present a maximum likelihood algorithm for estimating the model parameters, Θ , and inter-event and intra-event variance components, τ^2 and σ^2 . The algorithm is an iterative procedure in which the random effects, ϵ_i , variances, τ^2 and σ^2 , and model parameters, Θ , are computed successively using the expectation maximization algorithm described by Dempster and others (1977). The algorithm is very efficient because there are analytic expressions for estimating the random effects and variance components. However, it was discovered during the present analysis that Brillinger and Preisler's (1985) algorithm can yield spurious results if the starting estimate for the ratio τ^2/σ^2 is much larger than the "true" solution. Therefore, the log-likelihood expression, Equation (4), was maximized directly using numerical methods without explicitly estimating the random effects, ϵ_i . As the interest of the analysis was in evaluating the variance components, Equation (4) was maximized assuming the model parameters, Θ , are known. These were obtained by fitting Equation (1) to the data.

Using the attenuation relationship resulting from the fixed-effects model, the maximum likelihood estimates from the total data base (all magnitudes) for the inter-event and intra-event standard errors, τ and σ , are 0.368 and 0.516, respectively, yielding a total standard error of 0.634. The ratio τ/σ is 0.71, which is somewhat larger than the ratio of 0.52 obtained by Joyner and Boore (1981) and



Brillinger and Preisler (1985). The larger value for the ratio is likely due to the use of a larger data set for smaller magnitude earthquakes in this analysis than was used by Joyner and Boore (1981), as will be evident from the results presented below.

The model used in the above analysis assumes that the inter-event variations, ϵ_i , and the intra-event variations, ϵ_{ij} , are independent of each other. This assumption was checked by examining the correlation between the estimates of ϵ_i and ϵ_{ij} . The estimated correlation coefficient was 0.18. Therefore, the assumption of independence between ϵ_i and ϵ_{ij} is reasonable.

To investigate the dependence of the variance components on magnitude, the data were partitioned into overlapping half-magnitude ranges (the last interval consisted of one magnitude range because there was only one event of magnitude greater than 7). The maximum likelihood estimates of τ and σ and their standard errors of estimation for each magnitude range, together with the computed value of the total error, σ_T , and its standard error, are plotted against earthquake magnitude in Figure Q6-5. These results show a clear decreasing trend in both the inter-event, intra-event, and total dispersion with increasing magnitude. To make a preliminary check on the statistical significance of this trend, a linear relationship of the form

$$\begin{aligned}\tau(M) &= a_1 + b_1 M \\ \sigma(M) &= a_2 + b_2 M\end{aligned}\tag{5}$$

was fitted to the data using maximum likelihood. The hypothesis that the variance components are magnitude dependent was checked by using the likelihood ratio test (for example, Seber and Wild, 1989). The likelihood ratio test statistic, LR, is given by

$$LR = 2 [L(\phi) - L(\phi_0)]\tag{6}$$

where $L(\phi)$ is the log-likelihood (Equation 4) computed for a specified set of parameters, ϕ , and the test is of the hypothesis that ϕ equals a specified vector ϕ_0 . The LR statistic is approximately distributed as the chi-squared distribution when the hypothesis is true (Seber and Wild, 1989). Using the likelihood ratio test, the hypothesis that b_1 and b_2 are zero (that is, that τ and σ do not depend on magnitude) can be rejected at the 1-percent level, both when considering τ and σ separately and when considering them jointly.

Further examination of the trends shown in Figure Q6-5 indicates that the magnitude dependence of τ and σ is not linear. Accordingly they were modeled by a power law decreasing to a minimum value at magnitude M 6.8. That is

$$\tau(M) = \begin{cases} a_1 + b_1(M-3.5)^{c_1} & \text{for } M < 6.8 \\ \text{constant} & \text{for } M \geq 6.8 \end{cases}\tag{7}$$

and

$$\sigma(M) = \begin{cases} a_2 + b_2(M-3.5)^{c_2} & \text{for } M < 6.8 \\ \text{constant} & \text{for } M \geq 6.8 \end{cases}\tag{8}$$

As noted from Equations (7) and (8), the values of τ and σ for magnitudes greater than 6.8 were constrained to be the same as those computed for magnitude 6.8. This avoids estimating lower τ and σ values for larger magnitudes, where such estimates are not as well-constrained by the data.

The coefficients of Equations (7) and (8) were estimated by maximizing the log-likelihood function (Equation 4), again assuming the model parameters, Θ , were known. Having shown that the total dispersion (as shown in Figure Q6-5) was magnitude dependent, the model parameters, Θ , were redetermined from the data assuming the variance in ground-motions is magnitude dependent. Then, a weighted regression was performed on the data using weights inversely proportional to the square of the total error, σ_T , and using a linear approximation to the values of σ_T shown in Figure



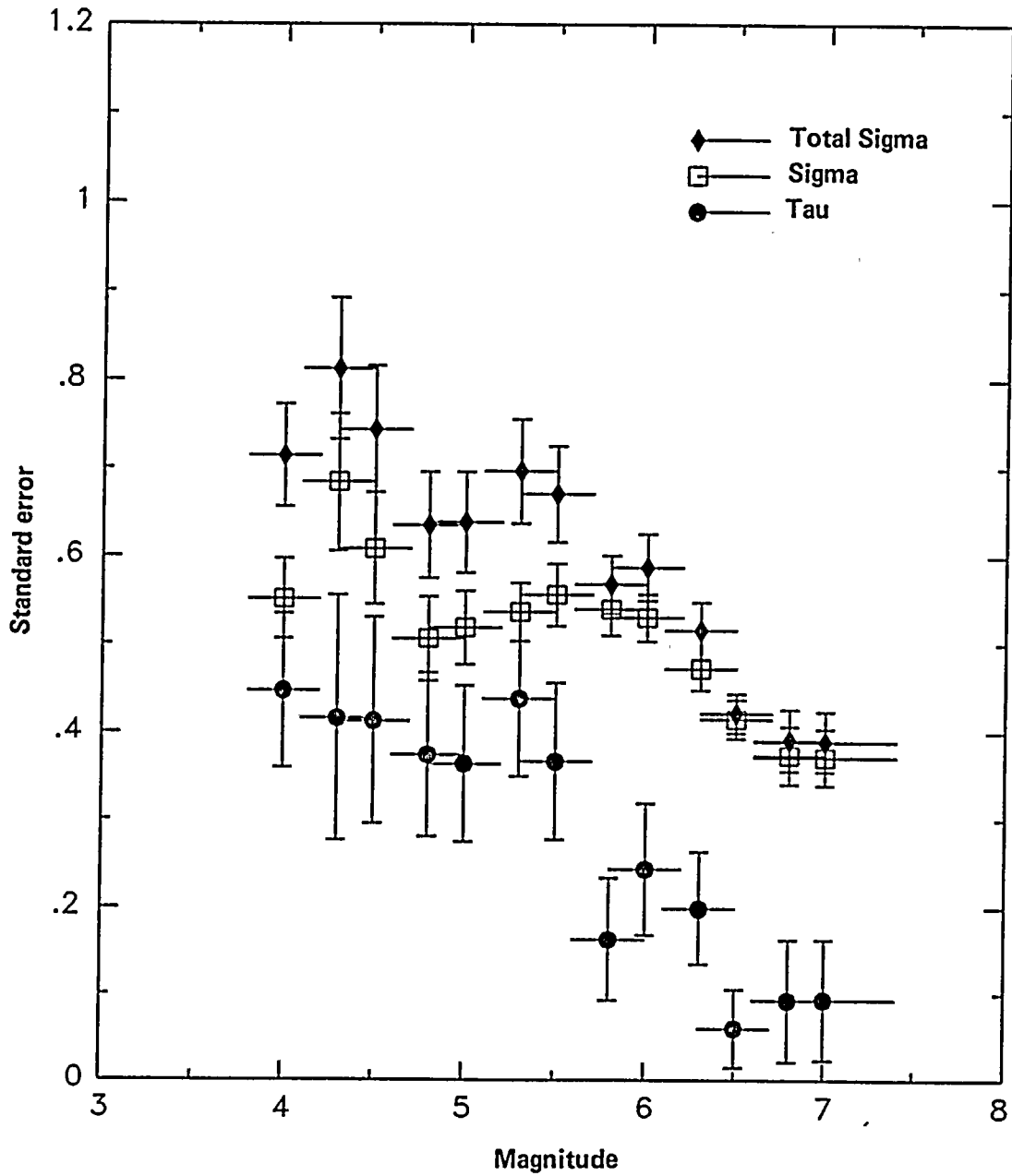


Figure Q6-5

Inter-event (τ), intra-event (σ), and total dispersion (σ_T) computed for half-magnitude bands. Vertical error bars show ± 1 standard error.



Q6-5. Also, a small number of recordings were downweighted due to their different tectonic setting and their topographic effects, as was done in our regression analyses and the statistical analyses of near-source recordings in the Final Report. The resulting median attenuation relationship is

$$\ln(a_{\max}) = -1.591 + 1.0M - 1.85\ln(R + 1.493\exp(0.386M)) + 0.24Z_r \quad (9)$$

The use of Equation (9) results in a slight reduction in the values of τ and σ computed for the half-magnitude bands shown in Figure Q6-5. The recomputed values are shown in Figure Q6-6, and are listed in Table Q6-1.

Figure Q6-6 shows the curves for the magnitude-dependent inter-event and intra-event dispersions resulting from fitting Equation (7) and (8) to the data. These curves compare well with the corresponding estimates for half-magnitude intervals computed using Equation (9). The results show that at small magnitudes, the inter-event and intra-event dispersions are about equal; at larger magnitudes, the intra-event dispersion dominates. It should be noted that inter-event variation for large magnitudes is small, but it is not underestimated. The small error bars for τ at large magnitudes shown in Figure Q6-6 indicate that τ is well-estimated for magnitudes up to M 6.8.

Figure Q6-7 shows the estimates of total dispersion resulting from combining the inter-event and intra-event dispersions shown in Figure Q6-6. Again the total dispersion, σ_T , shows a clear magnitude-dependent trend. It is interesting to note that the numerical simulations presented in response to Question 7 of this submission also indicate that the inter-event dispersion is significantly smaller than the intra-event dispersion for larger-magnitude earthquakes.

Conclusion

The magnitude dependence of the dispersion of peak ground-motion parameters is a statistically significant characteristic of strong ground motion, and is not an artifact of the data set. Such trends may be expected from the physics of the phenomenon; seismic motions due to large earthquakes will have contributions from various parts of the fault plane that will tend to average out the ground motions recorded at a site, resulting in less variability than motions from smaller earthquakes acting almost as point sources.

References

- Abrahamson, N. A., 1988, Statistical properties of peak ground accelerations recorded by the SMART 1 array: *Bulletin of the Seismological Society of America*, v. 78, p. 26-41.
- Brillinger, D. R., and Preisler, H. K., 1984, An exploratory analysis of the Joyner-Boore attenuation data: *Bulletin of the Seismological Society of America*, v. 74, p. 1441-1450.
- Brillinger, D. R., and Preisler, H. K., 1985, Further analysis of the Joyner-Boore attenuation data: *Bulletin of the Seismological Society of America*, v. 75, p. 611-614.
- Dempster, A. P., Laird, N. M., and Rubin, D. R., 1977, Maximum likelihood from incomplete data via the EM algorithm: *Journal of the Royal Statistical Society*, v. 39, p. 1-38.
- Idriss, I. M., Sadigh, K., and Power, M. S., 1982, Dependence of peak horizontal accelerations and velocities on earthquake magnitude at close distances to the source (Abstract): *Earthquake Notes*, v. 53.
- Joyner, W. B., and Boore, D. M., 1981, Peak horizontal acceleration and velocity from strong-motion records including records from the 1979 Imperial Valley, California earthquake: *Bulletin of the Seismological Society of America*, v. 71, p. 2011-2038.



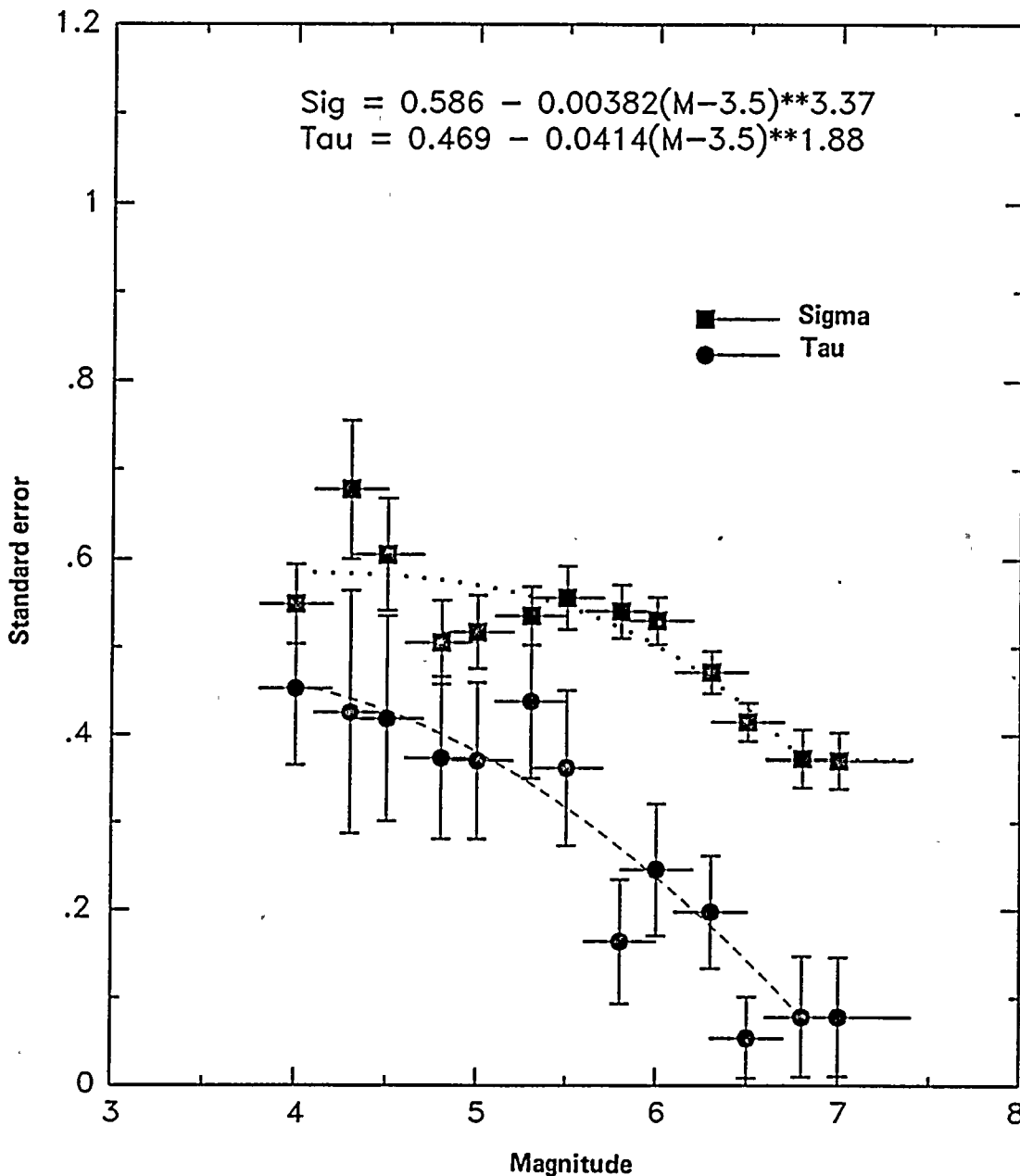


Figure Q6-6

Inter-event dispersion (τ) and intra-event dispersion (σ) (Table Q6-1), compared with the fitted curves of Equations (7) and (8).



Table Q6-1

INTER-EVENT (τ), INTRA-EVENT (σ), AND TOTAL (σ_T) DISPERSIONS
FOR SUBSETS OF THE DATA BASE COMPUTED USING FIXED EFFECTS EQUATION (9).

<u>Magnitude Band</u>	<u>Number of Earthquakes</u>	<u>Number of Records</u>	<u>τ</u>	<u>SE*τ</u>	<u>σ</u>	<u>SE*σ</u>	<u>σ_T</u>	<u>SE*σ_T</u>
3.8-4.2	35	106	0.453	0.088	0.550	0.045	0.717	0.059
4.1-4.5	23	59	0.426	0.139	0.678	0.077	0.812	0.080
4.3-4.7	23	67	0.418	0.118	0.605	0.063	0.744	0.072
4.6-5.0	23	77	0.373	0.093	0.506	0.048	0.634	0.060
4.8-5.2	20	96	0.370	0.090	0.517	0.042	0.641	0.058
5.1-5.5	21	150	0.439	0.089	0.536	0.033	0.697	0.060
5.3-5.7	20	139	0.362	0.089	0.557	0.036	0.669	0.054
5.6-6.0	18	172	0.164	0.071	0.541	0.030	0.570	0.033
5.8-6.2	15	203	0.246	0.075	0.530	0.027	0.589	0.038
6.1-6.5	11	203	0.198	0.064	0.472	0.024	0.515	0.032
6.3-6.7	8	185	0.055	0.046	0.415	0.022	0.421	0.022
6.6-7.0	4	65	0.079	0.069	0.374	0.033	0.388	0.034
6.6-7.4	5	68	0.078	0.068	0.371	0.033	0.385	0.033

* Standard error of estimation.



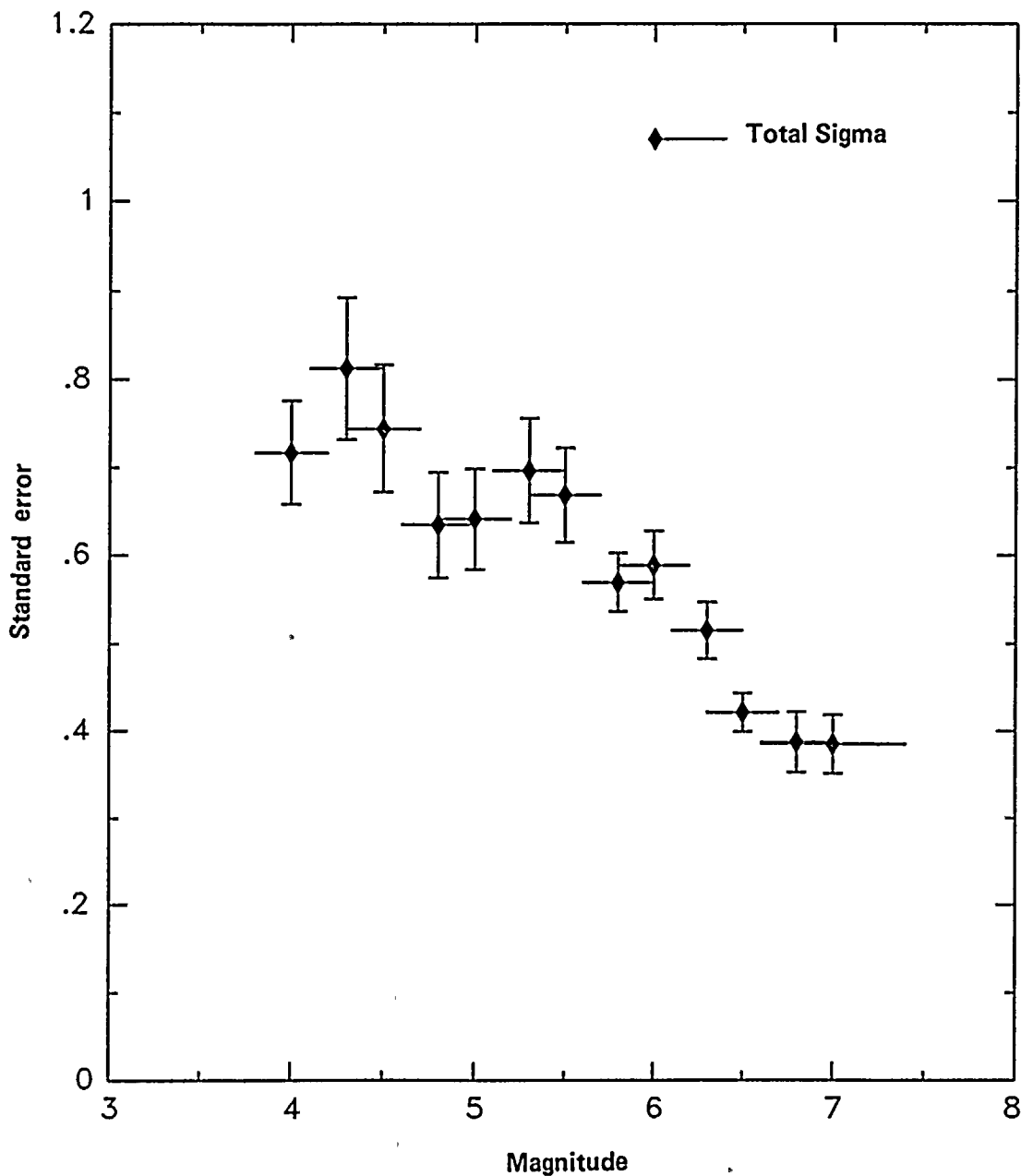


Figure Q6-7
Total dispersion (Table Q6-1).



Sadigh, K., 1983, Considerations in the development of site-specific spectra: Proceedings of Conference XXII; Site-Specific Effects of Soil and Rock on Ground Motions and the Implications for Earthquake Resistant Design, U.S. Geological Survey Open-File Report 83-845, p. 423-458.

Sadigh, K., Egan, J., and Youngs, R., 1986, Specification of ground motion for seismic design of long period structures (Abstract): Earthquake Notes, v. 57, no. 13.

Searle, S. R., 1971, Linear Models, John Wiley and Sons, New York.

Seber, G.A.F., and Wild, C.J., 1989, Nonlinear Regression, John Wiley and Sons, New York.





QUESTION 8

Show the effect of different assumptions of fault type (strike slip, oblique slip, and reverse slip) in the numerical modeling study.

The effect of fault type on ground motions was analyzed using the simulations described in the response to Question 17 of this submittal. The average peak acceleration and the response spectral acceleration averaged over the frequency band of 3 to 8.5 Hz for strike-slip, oblique, and thrust faults are summarized in Table Q8-1. For the oblique fault model, the peak acceleration and the averaged response spectral acceleration exceed those of the strike-slip fault model by 7 and 10 percent respectively. For the thrust fault model, the peak acceleration and the averaged response spectral acceleration exceed those of the strike-slip fault model by 16 and 19 percent respectively.

Table Q8-1

EFFECT OF FAULTING STYLE ON GROUND MOTIONS

<u>Faulting Style</u>	<u>Peak Acceleration</u>		<u>Response Spectral Acceleration (averaged from 3 to 8.5 Hz)</u>	
	<u>Absolute Value (g)</u>	<u>Relative to strike-slip</u>	<u>Absolute Value (g)</u>	<u>Relative to strike-slip</u>
Strike-Slip	0.351	1.0	0.795	1.0
Oblique	0.375	1.07	0.877	1.10
Thrust	0.406	1.16	0.948	1.19



Question 9

Provide a comparison between the numerical modeling study and the frequency-wave number method of the 1.5 km and 3 km source depth contributions.

Introduction

A comparison between the generalized ray Green's functions used in the simulations at the plant site and Green's functions computed using the frequency-wavenumber method for a source depth of 9.5 km was given in response to Question 13e, January 1989. The methods used and the equations for the Green's functions of both methods were given in that response. To respond to the present question, we make similar comparisons for source depths of 1.5 and 4.5 km (the depth of 3.0 km was not used in our simulations). We also compare averaged response spectra for suites of site simulations generated using the two different methods for calculating Green's functions.

In our simulation procedure using generalized rays, which was described in more detail in the response to Question 12, January 1989, we are able to separate the radiation pattern and receiver function from the simplified Green's functions of direct phases. This allows us to empirically incorporate the radiation pattern and receiver function by selecting from a set of empirical source functions that have been ranked in order of radiation pattern amplitude. In this way, we are able to empirically incorporate the incoherence in the radiation pattern that is observed at high frequencies.

Generally, it is not possible to separate the radiation pattern from Green's functions generated by frequency-wavenumber integration. This means that, when we use frequency-wavenumber integration, we are unable to implement the empirical representation of the radiation pattern and receiver function that was possible using generalized rays. However, for a vertical strike-slip fault, it is possible to separate the horizontal component of the radiation pattern from Green's functions calculated using frequency-wavenumber integration, and then empirically incorporate the horizontal component of the radiation pattern using the empirical source functions. The selection of the empirical source function is then based on its theoretical horizontal radiation pattern, rather than on its total radiation pattern. A consequence of this necessary difference in the way in which radiation pattern and receiver function are incorporated in the two simulation procedures is that a given fault element will in general be represented by a different empirical source function. These differences in source function selection contribute to the difference between the simulations generated using the two methods.

Simulation Procedure Using Green's Functions Computed by Frequency-Wavenumber Integration

The theoretical impulse response of a component of motion, u , can be represented as a sum of generalized ray contributions, u_i , of the form

$$u_i = \frac{d}{dt} \int [A_H(p)A_V(p)R(p)G(p)]_c$$

A_H and A_V are radiation pattern terms for a double couple that can be explicitly separated into a product of vertical and horizontal terms. $R(p)$ is a receiver function term that corrects for the effects of the free surface and transmutes displacement potential into displacement. $G(p)$ represents the effects of geometrical spreading and reflection coefficients between layers. All are evaluated along the complex contour, c , in the complex ray parameter, p , plane. Because any generalized ray can be decomposed in this fashion, we were able to implement our method of representing the product of $A_H(p) A_V(p) R(p)$ along with the effects of a source time history in the form of our empirical source functions.

The expression for displacement in terms of wavenumber integrals can not be decomposed in the same way. In this case,





$$u = \frac{A_H}{2\pi} \iint \omega^2 p U(\omega, p) e^{i(\omega pr - \omega t)} dp d\omega$$

The doubly transformed wave field is evaluated using reflectivity matrices, ω is frequency, p is k/ω where k is wavenumber, and r is the desired range for the synthetic seismogram. The exponential in pr is an asymptotic approximation to the more general Bessel function and we thus exclude the near-field term. The double integral is evaluated numerically. The p integration is evaluated using Filon quadrature and the frequency integration is performed with a fast Fourier transform. The horizontal radiation term can be factored out as indicated and, in the case of a vertical strike-slip earthquake, it takes the well known form of $A_H = \sin(2\Theta)$ for P and SV or $\cos(2\Theta)$ for SH energy. In the case of a shallow element, the effects of vertical radiation vary strongly within the numerical integrand because upgoing and downgoing energy has different radiation at the same (ω, p) point.

These differences require two major modifications of our simulation procedure, and inhibit an exact comparison of the simulated accelerograms using the generalized ray theory or the wavenumber integration method to compute the Green's functions. The first modification is to remove the effects of radiation pattern $A_V(p)$ and receiver function $R(p)$ from our empirical source functions. This is accomplished by making theoretical estimates of them from the Imperial Valley velocity structure. They were represented as real constants evaluated at p_0 for the fastest ray arriving at a given station, and were divided out from the empirical source functions. The second is to change our criterion for selecting an empirical source function. Instead of choosing the one whose theoretical total radiation pattern is closest to the desired value of the product of $A_H A_V$, we choose the one whose theoretical horizontal radiation pattern is closest to A_H .

Comparison of Simulation Procedures

At low frequencies, earthquake ground motions can be explained by coherent source and wave propagation effects. In this coherent regime, theoretical seismograms whose source models use a coherent double-couple radiation pattern and whose wave propagation models include coherent multiples provide adequate agreement with observed long-period ground motions. However, at the frequencies of importance at the plant site, strong ground motions are characterized by incoherent source and wave propagation phenomena, and these theoretical seismogram methods do not provide adequate representations of the high-frequency ground motions.

This indicates the need to adapt theoretical seismogram techniques to allow the inclusion of incoherent source and wave propagation effects. We selected the generalized ray method for calculating Green's functions in our simulation approach because it is more adaptable than other approaches to the incoherent regime of high-frequency strong ground motions. The adaptations that we have made are to empirically represent effects that are difficult to incorporate theoretically. The effectiveness of this approach in simulating recorded strong ground motions has been quantified in the response to Question 7 of the current submission, and we have shown in our response to Question 11 that it produces ground motions whose response spectra are dependable at frequencies of 2 Hz and above.

The comparison of this approach and the approach using frequency-wavenumber Green's functions described above is summarized in Table Q9-1. First, in our response to Question 12, January 1989, we showed that the radiation pattern loses coherence at high frequencies. It is therefore more appropriate to use an empirical representation of the radiation at high frequencies than to use a theoretical one. As described above, we are unable to separate the vertical component of the radiation pattern from Green's functions calculated by frequency-wavenumber integration. However, our simulation procedure allows the whole radiation pattern to be represented empirically, and is therefore preferable for the current applications. Second, by incorporating the receiver function empirically in the empirical source functions, we avoid the singular nature of the critical angle free surface reflection that results from theoretical calculations.





Table Q9-1

COMPARISON OF SIMULATION METHODS

	<u>Frequency-Wavenumber Method</u>	<u>Generalized Ray Method</u>
REGION OF APPLICATION	coherent domain; appropriate for frequencies below 2 Hz	incoherent domain; appropriate for frequencies above 2 Hz
RADIATION PATTERN	Vertical: theoretical Horizontal: empirical	Vertical: empirical Horizontal: empirical
RECEIVER FUNCTION	theoretical	empirical
MULTIPLES	theoretically included as coherent multiples; double counted as scattered energy in empirical source functions	empirically included as scattered energy in empirical source functions

Third, whereas direct waves are coherent at high frequencies, internal multiples tend to arrive as scattered arrivals rather than as coherent phases, because of lateral heterogeneity in the shallow crust. This scattered energy is present in our empirical source functions, as the only corrections made to them are for the direct wave. At high frequencies, the Green's functions calculated by frequency-wavenumber integration include internal multiples in an unrealistically coherent way; moreover, the multiples are effectively double-counted in the scattered energy contained in the empirical source functions. The approach we have used thus represents scattered energy more realistically than the approach using Green's functions calculated by frequency-wavenumber integration.

From this comparison of the two methods, it is apparent that their differences are not confined to differences between the methods used in calculating Green's functions. Additional differences relate to the degree to which each method can be adapted to represent the incoherent nature of the source and wave propagation at high frequencies, as summarized in Table Q9-1. In the following, when we refer to the "generalized ray" and "frequency-wavenumber" methods, we do so for brevity.

Comparison of Green's Functions

Green's functions calculated for the tangential component arrivals using the generalized ray and wavenumber integration methods for source depths of 1.5 and 4.5 km are shown on Figures Q9-1 and Q9-2. Overall, there is good correspondence between the large, high-frequency phases that represent the principal direct and reflected rays. These phases were identified in strong-motion recordings at the site. The lower-frequency waves that follow the shear wave arrivals in the frequency-wavenumber Green's functions are surface multiples; these waves are not included in the generalized ray Green's functions. For the 1.5-km source depth, these surface multiples have amplitudes approximately twice those of the diving direct wave in the distance range of 20 to 40 km; at a distance of 22.4 km, they arrive at 7 and 6 seconds, respectively. Their amplitudes are relatively large only for the 1.5-km source depth, and as we shall see in the following comparison, they do not contribute significantly in the ground-motion simulations.





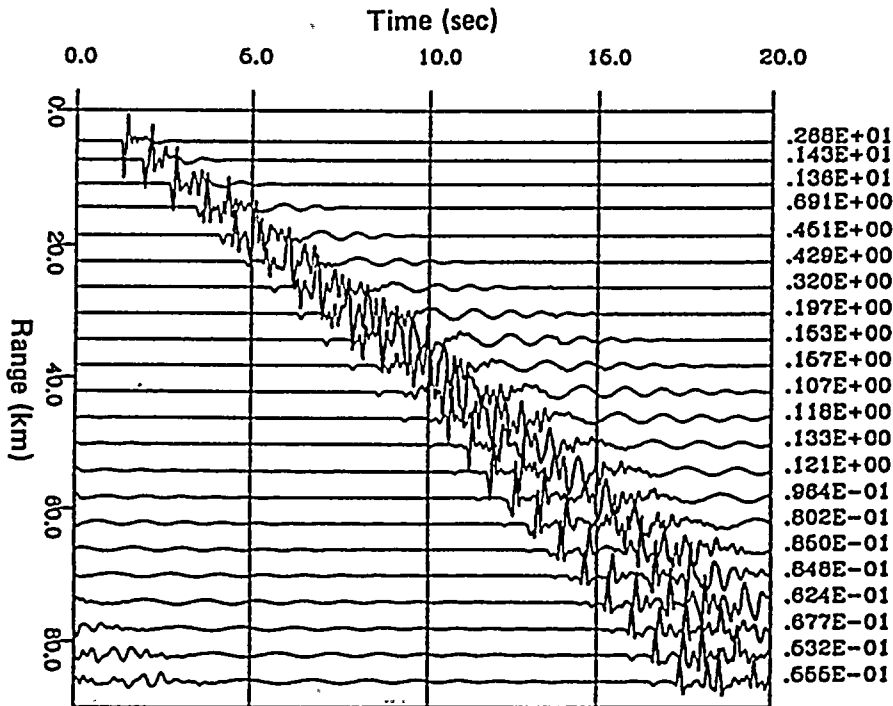
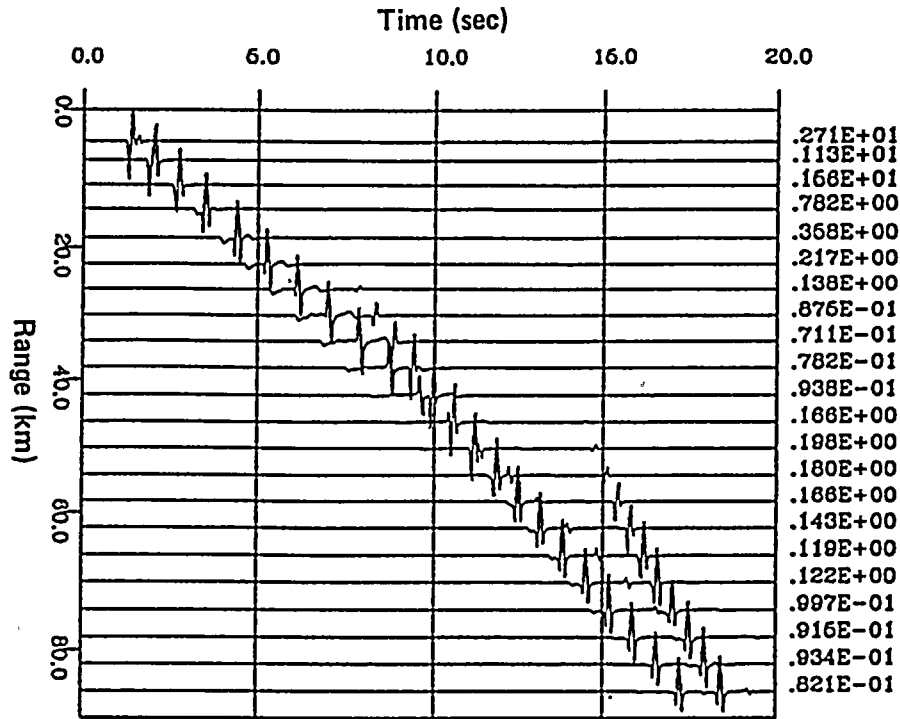


Figure Q9-1

Tangential component Green's functions for a source depth of 1.5 km calculated using generalized rays (above) and frequency-wavenumber integration (below).





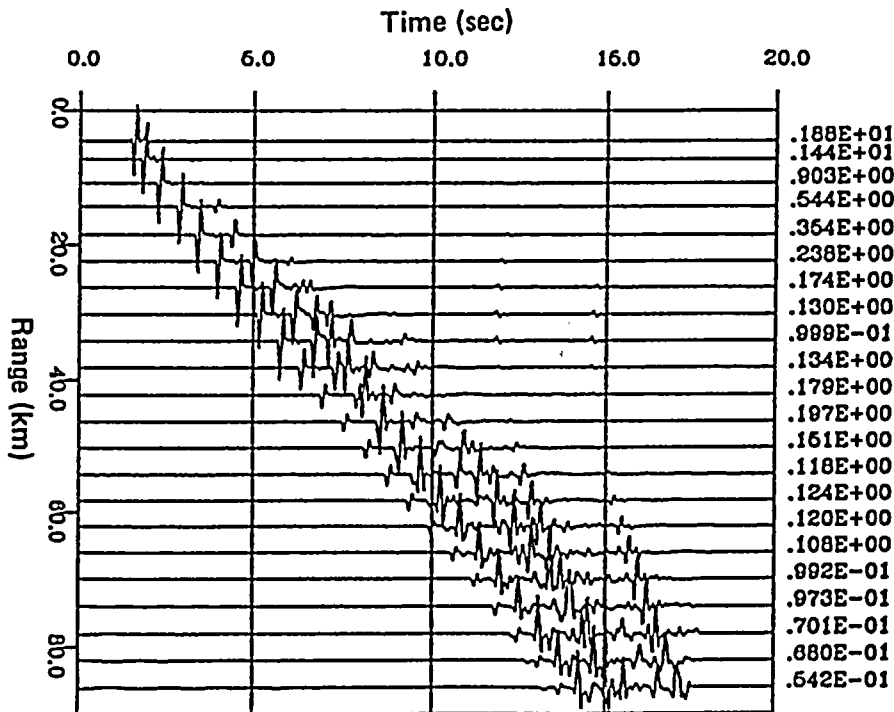
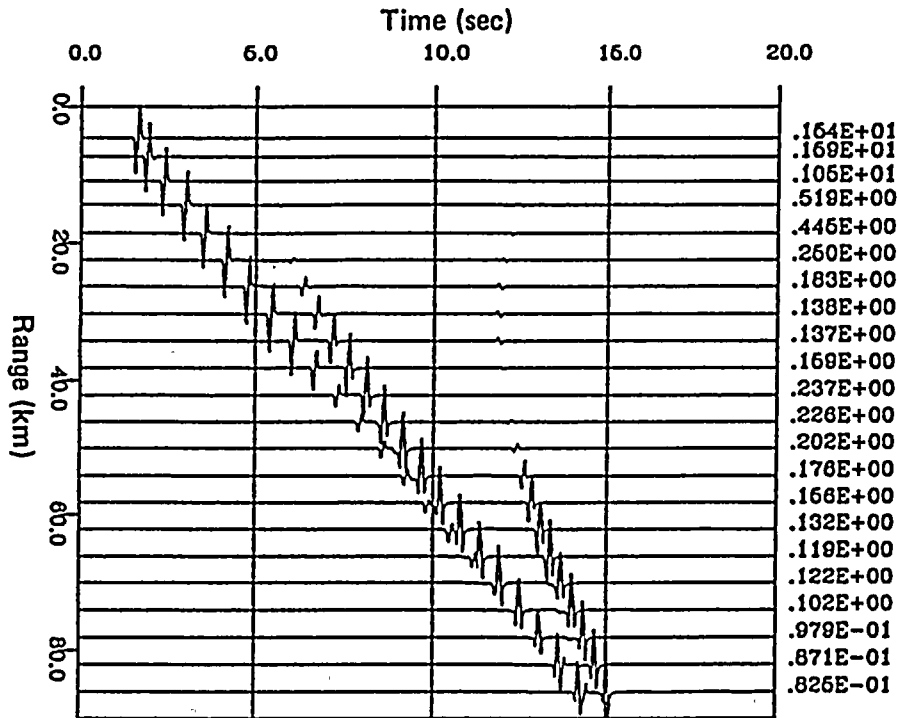


Figure Q9-2

Tangential component Green's functions for a source depth of 4.5 km calculated using generalized rays (above) and frequency-wavenumber integration (below).



Comparison of Simulation Results

A comparison of the averaged horizontal component response spectra of 22 strike-slip simulations using the two different methods is shown in Figure Q9-3. The agreement is very close, considering the fact that the computations of the Green's functions use completely independent approaches, and that the generalized ray method includes empirical representations of several incoherent phenomena that are treated coherently in the frequency-wavenumber method.

At frequencies below 2 Hz, the simulations generated using frequency-wavenumber Green's functions have larger response spectral amplitudes than those generated using generalized rays. This is because the former method includes surface multiples and the latter method does not. As ground motions below 2 Hz are relatively coherent, the simulations generated using frequency-wavenumber integration may be more realistic for frequencies below 2 Hz.

At frequencies above 2 Hz, there is generally good agreement between the response spectra generated using the two methods, and there is excellent agreement in peak acceleration. Even so, the generalized ray method is considered to give a more realistic result for frequencies above 2 Hz, because it uses a more adequate representation of the incoherence of the source and wave propagation effects that control strong ground motions at high frequencies, as summarized in Table Q9-1.

Conclusion

In our procedure for the simulation of ground motions at high frequencies, we have used empirical representations of several phenomena that are incoherent at high frequencies. One of these is to use the scattered energy in the empirical source functions to represent the effects of internal multiples, rather than to include them in the generalized ray Green's functions, because we do not expect them to be coherent phases at high frequencies. The main differences between the Green's functions calculated using the generalized ray and frequency-wavenumber methods are due to the coherent representation of multiples in the latter. The effect of these differences on the simulated motions is mainly confined to frequencies below 2 Hz, where the assumption of coherence in source and wave propagation effects in the frequency-wavenumber approach is more appropriate. Above 2 Hz, the differences between the ground motions simulated by the two methods are generally small. At these frequencies, the generalized ray approach, which allows the empirical representation of incoherence in source and wave propagation effects, is appropriate for our applications.



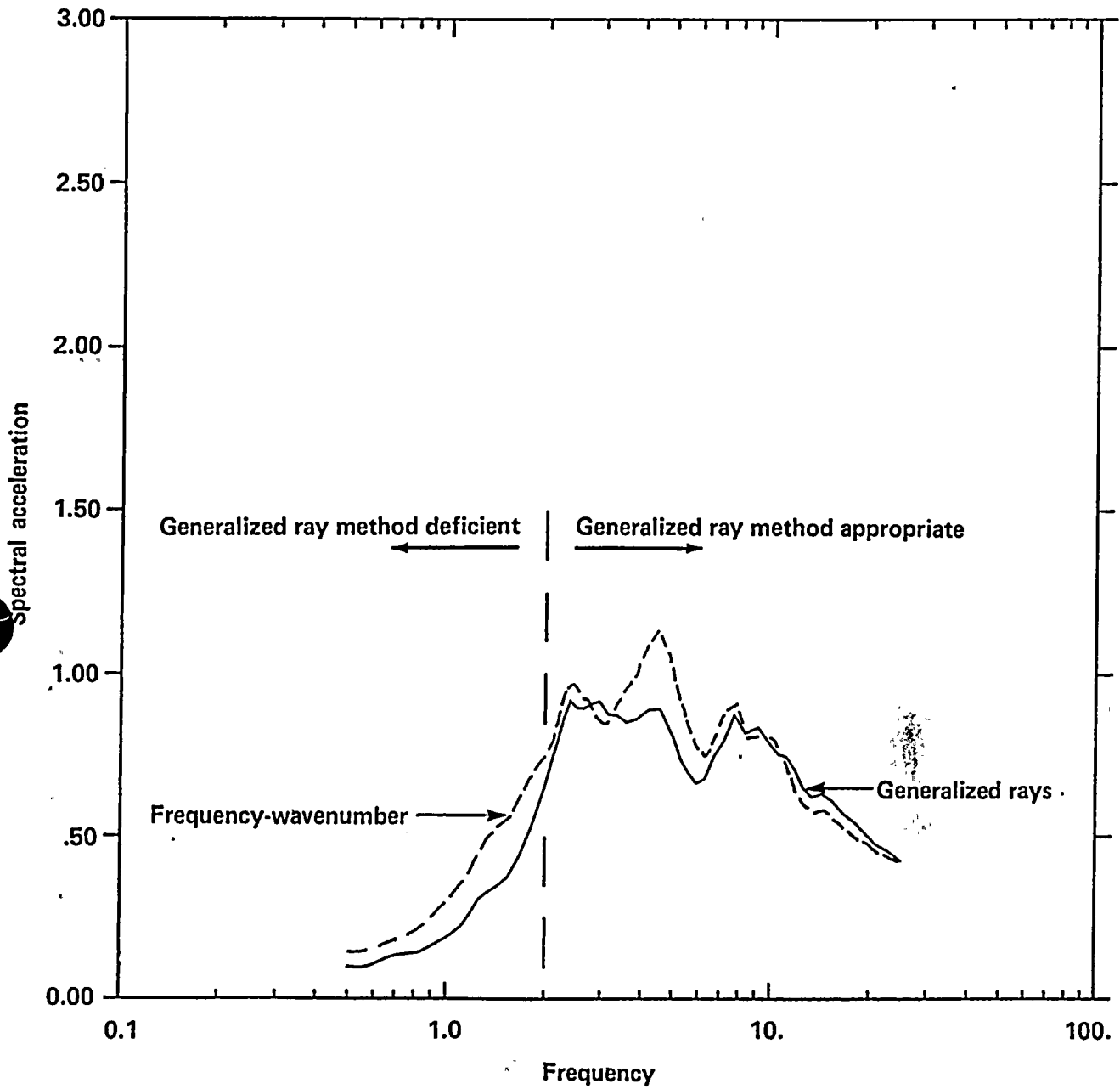


Figure Q9-3

Averaged response spectrum of 22 strike-slip simulations generated using two different methods.





QUESTION 15

The derivation of the various adjustment factors used to modify the empirical ground motion and their individual effects have not been described in sufficient detail to permit an evaluation of their appropriateness. Please provide this information.

The derivation of the various adjustment factors used to modify the empirical ground motion and their individual effects have been presented in several submittals and presentations in the past 3 years. In response to this question, we will summarize the details and tabulate the various scaling factors used to modify individual recordings. In addition to these scaling factors, adjustments were made to a few near-source records using weighting factors. Each weighting factor reflects the overall compatibility in seismic environment between a recording site and the plant site, as described in response to Question 9, January 1989.

As a part of the empirical ground-motion investigations, site-specific response spectra were developed based on the attenuation relationships developed by regression, and also based on statistical analysis of near-source strong-motion records. The data base selected for the statistical analysis consists of a suite of 18 records from earthquakes having moment magnitudes from 6.3 to 7.4, and source-to-site distances ranging from 3 to 20 km. Eleven records are from thrust earthquakes, and seven records are from strike-slip earthquakes. Thirteen records are from rock or rock-like sites, and five records are from soil sites.

Before conducting the statistical analysis of these near-source records, they were adjusted, if necessary, to be compatible with site-specific conditions at Diablo Canyon; namely, they were adjusted to (1) a moment magnitude of 7.2, (2) a source-to-site distance of 4.5 km, (3) rock-site conditions, and (4) a common style of faulting. Described below are the various adjustment factors used to modify the records for distance and magnitude, local site conditions, and style of faulting. As noted below, several published empirical and numerical ground motions studies, as well as the results of the Long Term Seismic Program's empirical and numerical ground-motion investigations, have been used in selecting the various adjustment factors.

Adjustment Factors for Distance and Magnitude

The studies used in developing adjustment factors for distance and magnitude consisted of the following empirical studies:

Joyner and Boore (1981, 1982)
Campbell (1981, 1987, 1988)
Sadigh and others (1986)
Seed and Schnabel (1980)
Long Term Seismic Program

In addition, the results of selected numerical simulations were used as a guide:

Hadley and Helmberger (1980)
Hadley and others (1982)
Long Term Seismic Program

The various empirical relationships are summarized and compared in Figure Q15-1, (Figure Q9-1, January 1989) for a magnitude 7 earthquake at the distance range of interest to this study, between 2 and 20 km. The attenuation relationship selected for scaling the near-source recordings is shown by the solid line in Figure Q15-1 (based on the results of the regression analyses). Similar relationships were used for scaling for other magnitudes. The scaling relationships for magnitudes 6.5, 7.0, 7.2, and 7.5 in the distance range of 2 to 20 km are presented in Figure Q15-2 (Figure



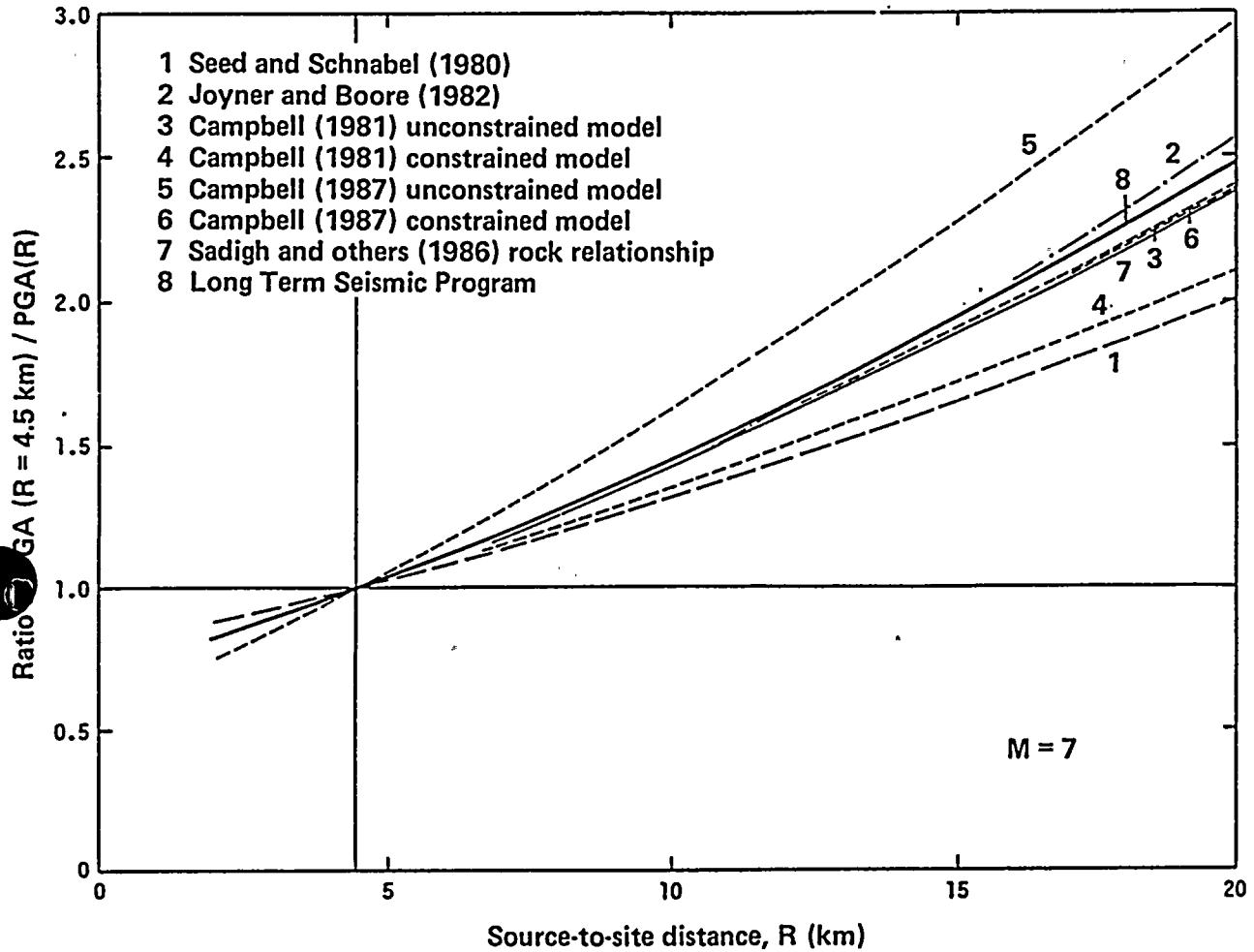


Figure Q15-1

Various empirical scaling relationships for magnitude and distance.



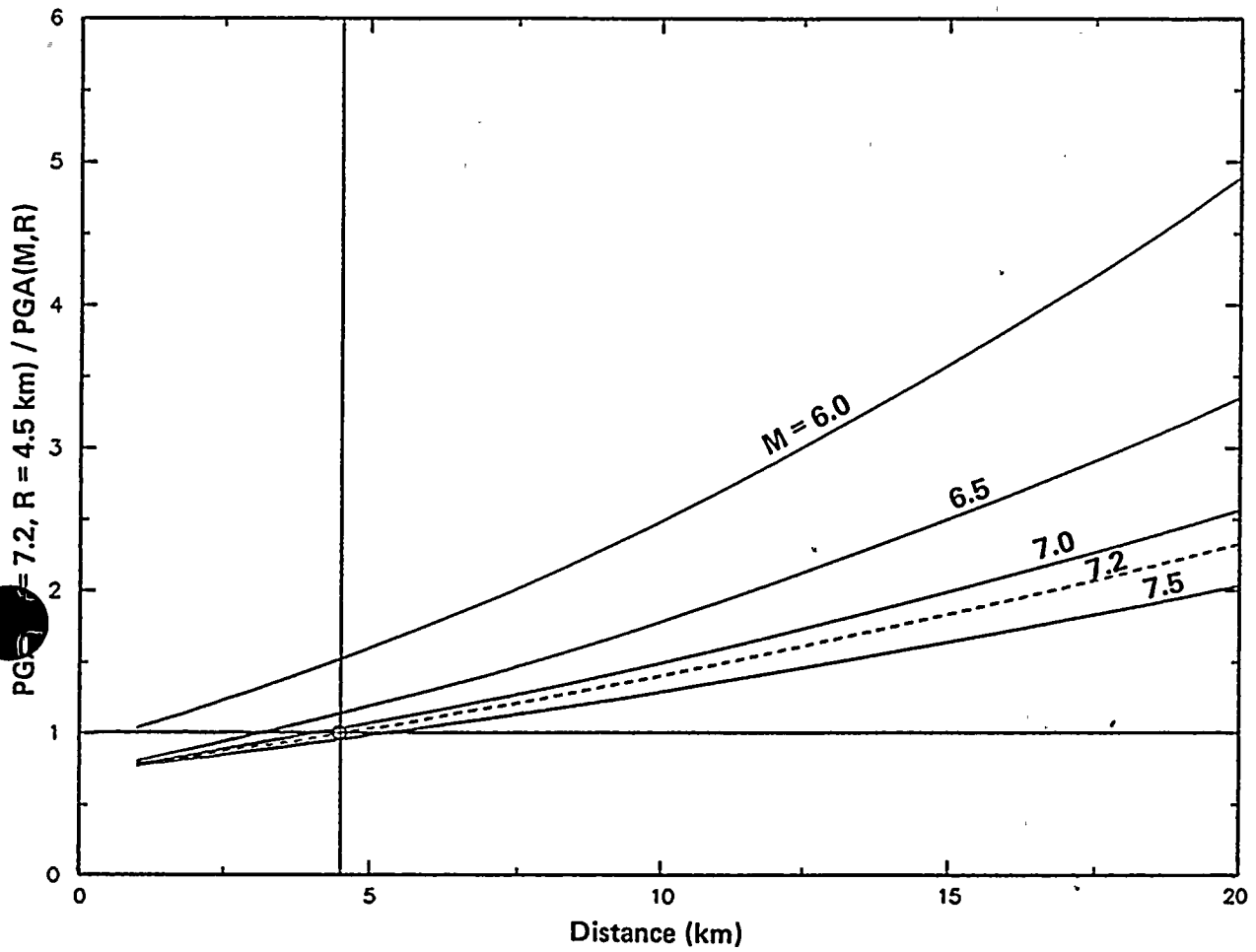


Figure Q15-2

Scaling relationships for magnitude and distance used for near-source records.



Q9-2, January 1989). The scaling factors in this figure have been calculated relative to a moment magnitude of 7.2 and a source-to-site distance of 4.5 km. For example, to estimate the adjustment factor used to scale the Tabas-Dayhook record, from a magnitude 7.4 earthquake at a source-to-site distance of 17 km, one can use the graph in Figure Q15-2 to read the scaling factor corresponding to $M = 7.4$ and $R = 17$ km, which is 1.86. Similar adjustment factors for the other near-source records were obtained in the same manner and are presented in the column labeled "Adjustment Factors for PGA to $M 7.2, R = 4.5$ " in Table Q15-1.

Figure Q15-3 provides a comparison of the peak ground acceleration scaling relationships for magnitude and distance used for the near-source records in our statistical study with the scaling relationships derived using the attenuation relationship from the recent study by Campbell (1988), contained in his report to the NRC. The magnitude and distance scaling factors for peak ground acceleration from these two studies are in close agreement.

In addition to the effect of magnitude on peak ground acceleration, adjustments were also made to spectral shape as a function of magnitude. Figure Q15-4 (Figure Q8-15, January 1989) shows the effect of magnitude on response spectral shape for magnitudes 6.5, 7, and 7.5. The effect of magnitude on spectral shape selected for modifying the near-source records in our statistical study was based on the results of the regression analyses, as presented in our response to Question 8, January 1989. It may be seen that the spectral acceleration in the longer period range (lower frequency range) increases with increasing magnitude.

The effects of adjustments due to magnitude-dependent spectral shape for the 18 near-source records are not significant, as reflected by the factors for spectral acceleration in the 3 to 8.5 Hz range in Table Q15-1 (in the column labeled "Additional Adjustment"). The scaling factors for the 18 records ranged between 0.99 and 1.06.

Adjustment Factors for Site Conditions

For adjustments due to the effects of site conditions, two relationships are usually considered; one dealing with the effect on peak ground acceleration, the second dealing with the effect on the spectral acceleration ordinates. Evidence from empirical studies of ground motions has shown consistent differences between ground motions recorded on rock sites and those recorded on soil sites. These differences have been reported by several authors, for example, Hayashi and others (1971) and Kuribayashi and others (1972) in Japan, and by Seed and others (1976), Mohraz (1976), Trifunac (1976), Boore and others (1980), Joyner and Boore (1981), Sadigh (1983; 1984), Sadigh and others (1986), Seed and Idriss (1982), Seed (1986), and Aki (1988) for earthquakes in the western United States.

The adjustment factors for the effects of site conditions selected for the Long Term Seismic Program are:

- Adjustment for effects on peak ground acceleration. Relationships relating peak ground acceleration at soil and rock sites are shown in Table Q15-2 (Table Q9-1, January 1989). Based on these relationships, a scaling factor of 1.15 was selected to multiply the peak ground acceleration and all spectral accelerations recorded at a soil site to modify them to rock-site conditions, that is, the entire response spectrum was scaled upwards by a factor of 1.15.
- Adjustment for effects on spectral shape. Relationships relating spectral acceleration shapes between soil and rock sites are shown in Figure Q15-5 (Figure Q9-3, January 1989) for three studies reported in the literature. The figure shows the relationship between normalized spectral accelerations of soil and those of rock sites as a function of frequency. Thus, in addition to the scaling factor of 1.15 described above, the response spectral shapes of recordings obtained from soil sites were further modified to rock-site spectral shapes using the relationships shown by the dashed line in Figure Q15-5. As can be seen, the scaling factors used result in an increase



Table Q15-1

CHARACTERISTICS OF RECORDS USED IN STATISTICAL ANALYSES OF
NEAR-SOURCE GROUND MOTIONS

Earthquake/Record Name	Style of Faulting	Magnitude Mw	Distance Km	Original PGA-g	Original (Sa) 3-8.5 Hz	Adjustment Factors for PGA			Total Adjust-ment Factor	Adjusted PGA (g's)	Adjustment Factors for (Sa) 3-8.5 Hz		Adjusted (Sa) 3-8.5 Hz
						To M7.2, R=4.5	To "Rock Site" Condition	To Strike-slip			Additional + Adjustment	Total Adjust-ment Factor	
ROCK SITES													
1 Gasli/Karakyv Point	Thrust	6.8	3	0.70 0.66	1.311 1.328	0.947	1.0	0.833	0.789	0.552 0.521	1.01	0.797	1.045 1.058
2 Tabas/Tabas	Thrust	7.4	3	0.70 0.81	2.441 2.221	0.883	1.0	0.833	0.736	0.515 0.596	0.99	0.729	1.779 1.619
3 San Fernando/Pacoina	Thrust	6.6	3	1.08 1.17	1.884 1.944	0.974	1.0	0.833	0.544**	0.587 0.636	1.02	0.827	1.558 1.608
4 Koyna/Koyna Dam	Strike-slip	6.3	3	0.63 0.49	1.171 0.713	1.103	1.0	1.0	1.103	0.695 0.540	1.06	1.169	1.369 0.833
5 Wahanni/Site 1	Thrust	6.8	6	1.35 1.10	1.792 2.145	1.204	1.0	0.833	1.003	1.354 1.103	1.00	1.003	1.797 2.151
6 Wahanni/Site 2	Thrust	6.8	8	0.59 0.42	0.507 0.497	1.394	1.0	0.833	1.161	0.685 0.488	1.00	1.161	0.589 0.577
7 Tabas/Dayhook	Thrust	7.4	17	0.39 0.38	0.652 0.951	1.865	1.0	0.833	1.554	0.606 0.591	0.99	1.538	1.003 1.463
8 Wahanni/Site 3	Thrust	6.8	16	0.19 0.19	0.189 0.221	2.299	1.0	0.833	1.915	0.364 0.364	1.00	1.915	0.362 0.423
9 San Fernando/Lankershim Blvd.	Thrust	6.6	15	0.18 0.15	0.358 0.390	2.384	1.0	0.833	1.986	0.357 0.298	1.02	2.026	0.725 0.790
10 San Fernando/Griffith Park Observatory	Thrust	6.6	17	0.19 0.18	0.381 0.410	2.683	1.0	0.833	2.235	0.425 0.402	1.02	2.280	0.869 0.935
11 San Fernando/Old Seismology Lab - CIT	Thrust	6.6	19	0.10 0.20	0.255 0.511	3.000	1.0	0.833	2.499	0.250 0.500	1.02	2.549	0.650 1.303
12 San Fernando/Lake Hughes #12	Thrust	6.6	20	0.37 0.29	0.922 0.875	3.166	1.0	0.833	2.637	0.976 0.765	1.02	2.690	2.480 2.354
13 Mexicali Valley	Strike-slip	6.4	8.5	0.60 0.61	0.649 0.968	1.698	1.0	1.0	1.698	1.019 1.036	1.05	1.783	1.157 1.783
SOIL SITES													
14 Imperial Valley/Differential Array	Strike-slip	6.5	5	0.49 0.35	1.043 1.087	1.18	1.15	1.0	1.357	0.665 0.475	1.03	1.398	1.458 1.520
15 El Centro No. 4	Strike-slip	6.5	4	0.49 0.37	0.909 0.609	1.09	1.15	1.0	1.254	0.614 0.464	1.03	1.292	1.174 0.787
16 Holtville Post Office	Strike-slip	6.5	7.5	0.26 0.22	0.580 0.678	1.40	1.15	1.0	1.610	0.419 0.354	1.03	1.658	0.962 1.124
17 El Centro No. 10	Strike-slip	6.5	8.5	0.23 0.18	0.536 0.412	1.50	1.15	1.0	1.725	0.397 0.311	1.03	1.777	0.952 0.737
18 El Centro No. 8	Strike-slip	6.5	4	0.62 0.48	0.972 0.934	1.09	1.15	1.0	1.254	0.777 0.602	1.03	1.292	1.256 1.207

* Adjustment factor in addition to that applied to peak ground acceleration
 ** Includes adjustment factor of 0.67 for topographic effects



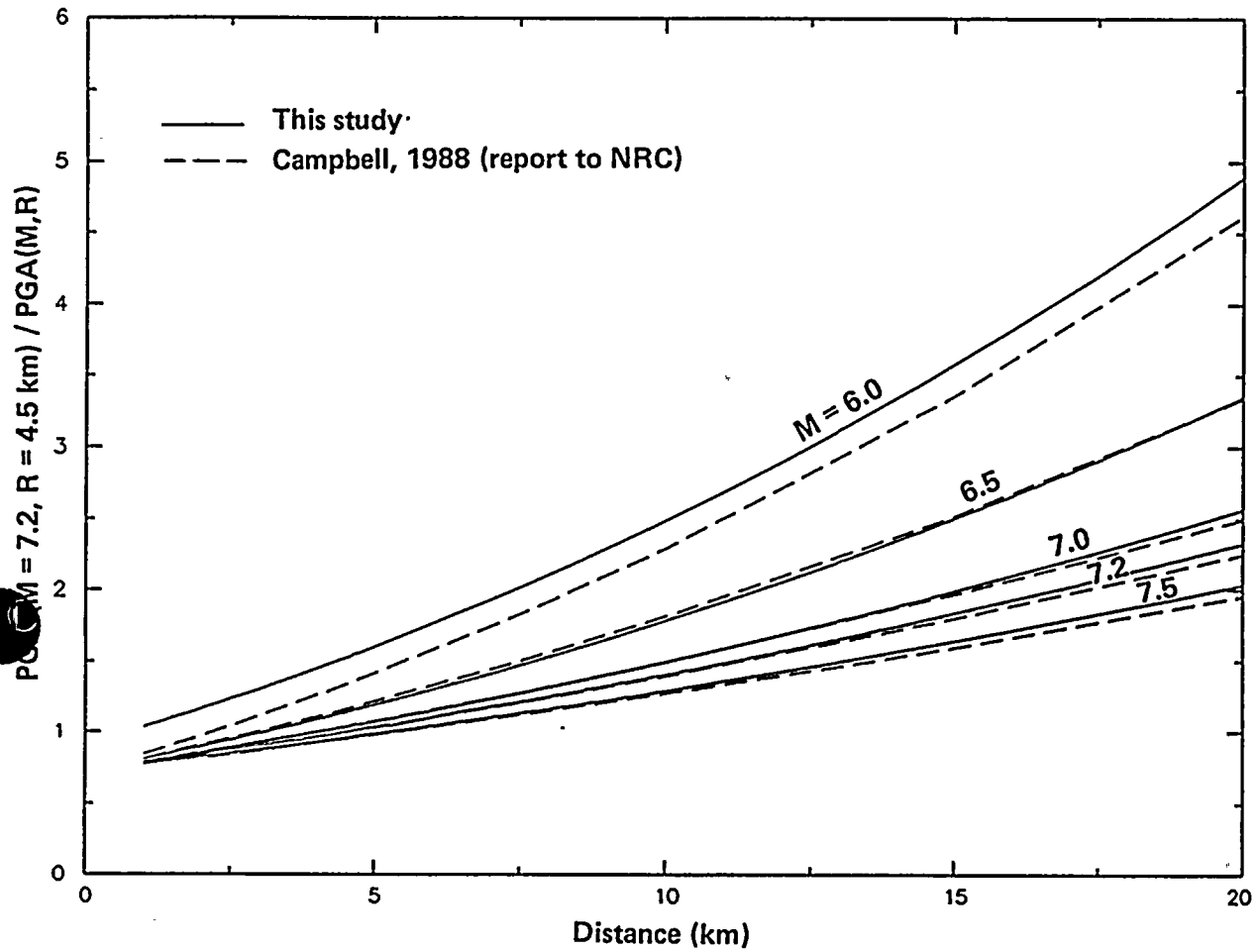


Figure Q15-3

Scaling relationships for magnitude and distance used for near-source records compared with Campbell's (1988) relationships.



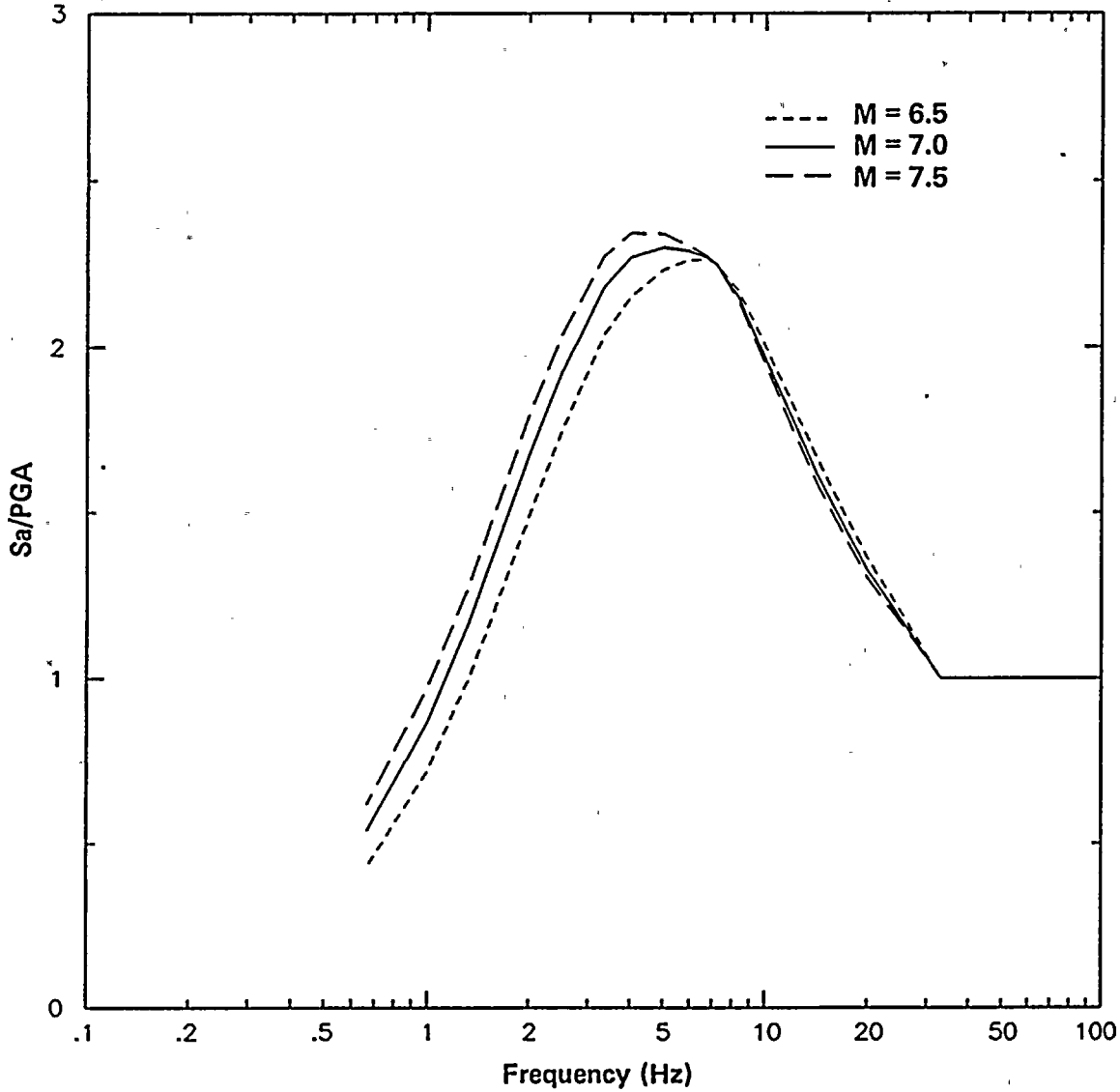


Figure Q15-4

Effects of magnitude on response spectral shapes.



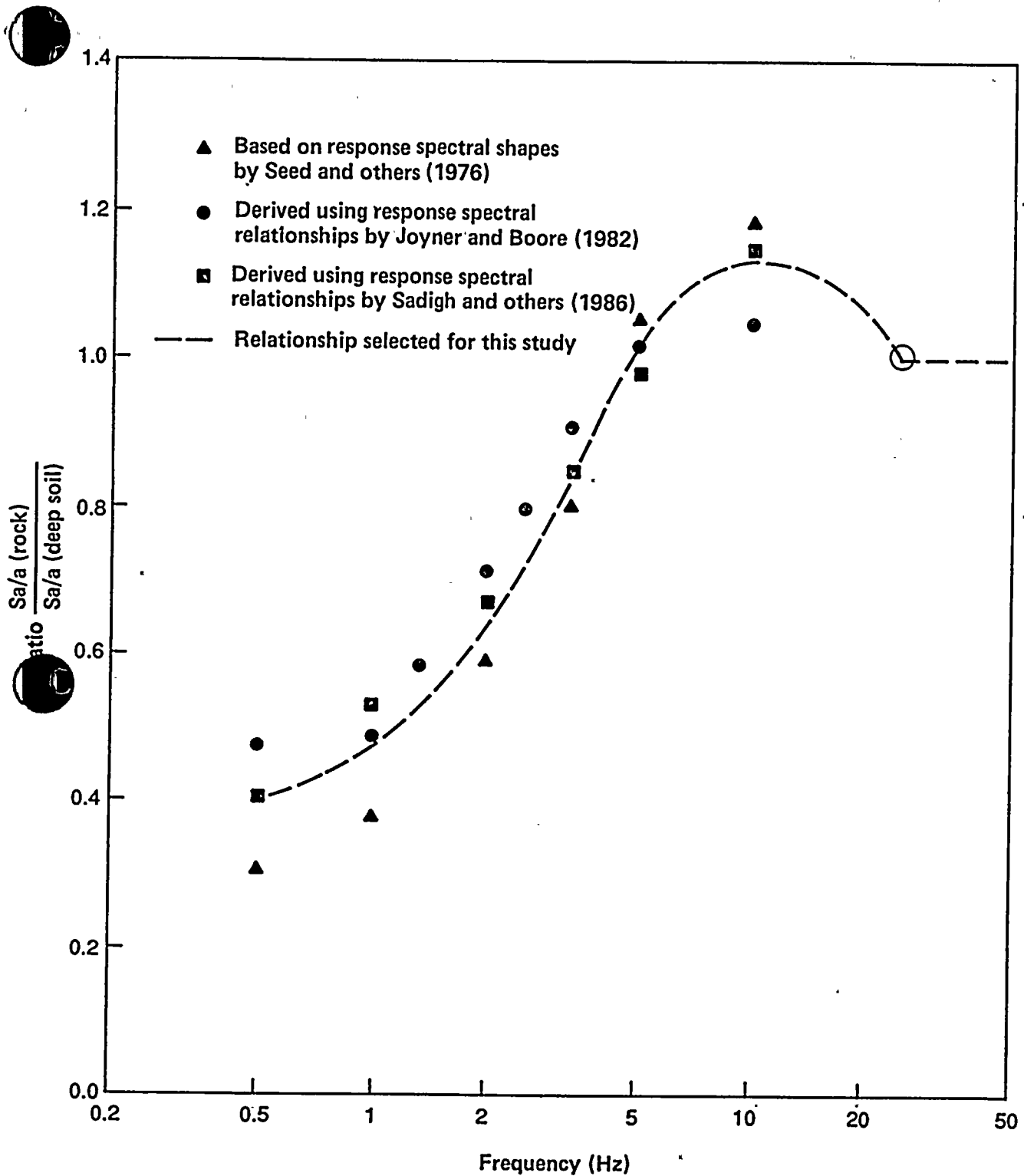


Figure Q15-5

Spectral acceleration shape relationships between soil and rock sites.



Table Q15-2

**SCALING RELATIONSHIPS FOR PEAK GROUND ACCELERATION
FOR ROCK-SITE CONDITIONS**

<u>Relationships</u>	<u>Ratio of PGA for rock sites to PGA for soil sites</u>
Joyner and Boore (1981)	1.0
Campbell (1981)	1.0
Seed and Idriss (1982)	1.3 (for PGA 0.3 to 0.5 g)
Sadigh and others (1986)	1.25 (for PGA 0.3 to 0.5 g)
<u>Selected for Long term Seismic Program</u>	<u>1.15</u>

in spectral acceleration in the high-frequency range (5 to 25 Hz), and a reduction at frequencies less than 5 Hz.

An example of the application of the adjustment factors is illustrated in Figure Q15-6 for the Differential Array recording of the 1979 Imperial Valley earthquake. The original spectrum shown by the dotted line (curve 1) is scaled by 1.15 throughout the frequency range and is shown by the dashed line (curve 2). Then the relationship shown in Figure Q15-5 was used to modify the spectral shape to that representative of rock-site conditions. The modified spectrum is shown by the solid line (curve 3) in Figure Q15-6. As can be seen from comparison of curves 1 and 3, the adjustment to rock-site conditions results in an increase in spectral acceleration at frequencies above 3 Hz, and a reduction at frequencies less than about 3 Hz.

Adjustment Factors for Style of Faulting

Quantification of the effect of style of faulting on peak ground acceleration was based on literature review, analysis of soil and rock data sets, and numerical modeling results (Table Q15-3). Details regarding the empirical and numerical ground-motion studies made to quantify the effect of style of faulting on peak ground acceleration are presented in our response to Question 17 of this submittal. On the basis of these analyses, a factor of 1.2 was selected to scale recordings from a strike-slip faulting mechanism so they would correspond to those from thrust faulting. Conversely, a factor of 0.833 was used to scale recordings from thrust to strike-slip, as shown in Table Q15-1, for example. The site-specific spectrum obtained from the statistics of these near-source recordings was then scaled to the appropriate style of faulting based on the relative probabilities of occurrence of each faulting mechanism.



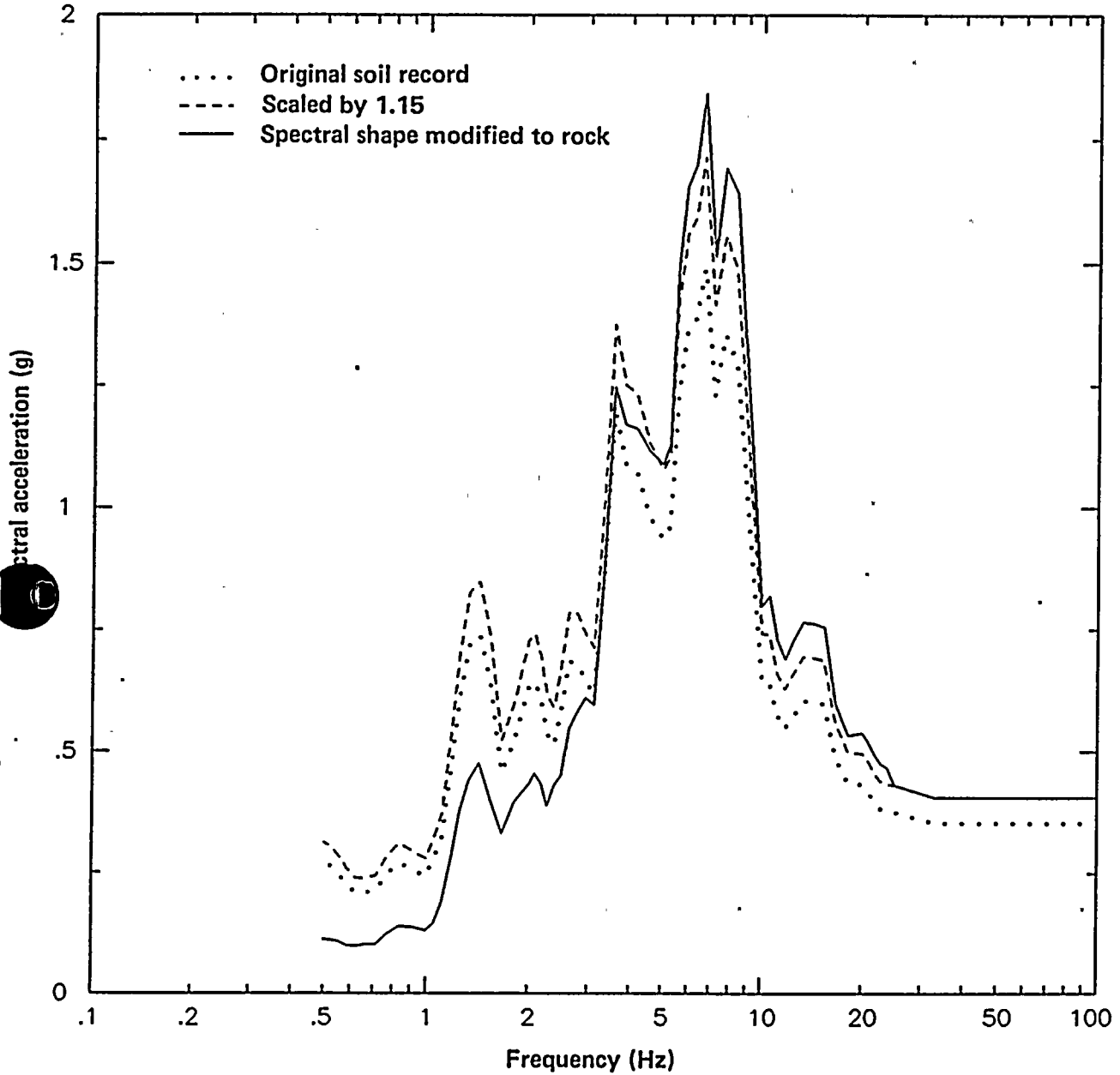


Figure Q15-6

Imperial Valley Differential Array recording modified to rock-site conditions.



Table Q15-3

EFFECT OF STYLE OF FAULTING ON PEAK GROUND ACCELERATION

<u>Empirical Relationships</u>	<u>Ratio of PGA for Thrust Faulting to PGA for Strike-Slip Faulting</u>
Campbell (1981)	1.17 - 1.28
Campbell (1987)	1.38 - 1.40
Campbell (1988)	1.46
Long Term Seismic Program	
All magnitudes (M 4.8 to 7.4)	1.27
Magnitude 6.3 or greater	1.22
 <u>Numerical Simulations</u>	
Boore and Boatwright (1984)	1.14 - 1.28
Long Term Seismic Program	1.16
 <u>Selected for Long Term Seismic Program</u>	 <u>1.2</u>





References

Aki, K., 1988, Local site effects on ground motions, in *Earthquake Engineering and Soil Dynamics II - Recent Advances in Ground Motion Evaluation*, ASCE Geotechnical Engineering Specialty Conference, Park City, Utah.

Boore, D. M., and Boatwright, J. A., 1984, Average body-wave radiation coefficients, *Bulletin of the Seismological Society of America*, v. 74, p. 1615-1621.

Boore, D. M., Joyner, W. B. Oliver, A. A., III, and Page, R. A., 1980, Peak acceleration, velocity, and displacement from strong motion records, *Bulletin of the Seismological Society of America*, v. 70, p. 305-321.

Campbell, K. W., 1981, Near-source attenuation of peak horizontal acceleration, *Bulletin of the Seismological Society of America*, v. 71, p. 2039-2070.

Campbell, K. W., 1987, Predicting strong ground motion in Utah: in *Assessment of Regional Earthquake Hazards and Risk along the Wasatch Front, Utah*, U.S. Geological Survey Open File Report 87-585, v. 2, p. L1-L90.

Campbell, K. W., 1988, Preliminary report on empirical studies of horizontal strong ground motion for the Diablo Canyon site, California, Report to the U.S. Nuclear Regulatory Commission, October 1988.

Hadley, D. M., and Helmberger, D. V., 1980, Simulation of strong ground motions, *Bulletin of the Seismological Society of America*, v. 70, p. 959-968.

Hadley, D. M., Helmberger, D. V., and Orcutt, J. A., 1982, Peak acceleration scaling studies, *Bulletin of the Seismological Society of America*, v. 72, p. 959-979.

Hayashi, S., Tsuchida, H., and Kurata, E., 1971, Average response spectra for various subsoil conditions, Third Joint Meeting, US-Japan Panel on Wind and Seismic Effects, UJNR, Tokyo.

Joyner, W. B., and Boore, D. M., 1981, Peak horizontal acceleration and velocity from strong-motion records including records from the 1979 Imperial Valley, California, earthquake, *Bulletin of the Seismological Society of America*, v. 71, p. 2011-2038.

Joyner, W. B., and Boore, D. M., 1982, Prediction of earthquake response spectra, U.S. Geological Survey Open File Report 82-977.

Kuribayashi, E., Iwasaki, T., Iida, Y., and Tuji, K., 1972, Effects of seismic and subsoil conditions on earthquake response spectra, *Proceedings of the International Conference on Microzonation*, p. 499-512.

Mohraz, B., 1976, A study of earthquake response spectra for different geological conditions, *Bulletin of the Seismological Society of America*, v. 66, p. 915-935.

Sadigh, K., 1983, Considerations in the development of site-specific spectra, in *Proceedings of Conference XXII, Site-specific Effects of Soil and Rock on Ground Motion and the Implications for Earthquake Resistant Design*, U.S. Geological Survey Open File Report 83-845.

Sadigh, K., 1984, Characteristics of strong motion records and their implications for earthquake resistant design, presented at EERI Seminar 12, Stanford, California.

Sadigh, K., Egan, J. A., and Youngs, R. R., 1986, Specification of ground motion for seismic design of long period structures, *Earthquake Notes*, v. 57, no. 1, p. 13.





Seed, H. B., 1986, Influence of local soil conditions on ground motions and building damage during earthquakes, Eighth Nabor Carillo Lecture, XIII National Meeting of the Mexican Society for Soil Mechanics, Mazatlan, Mexico.

Seed, H. B., and Idriss, I. M., 1982, Ground motions and soil liquefaction during earthquakes, in Engineering Monographs on Earthquake Criteria, Structural Design, and Strong Motion Records, v. 5, Earthquake Engineering Research Institute.

Seed, H. B., and Schnabel, P., 1980, published in Ground Motions and Soil Liquefaction During Earthquakes, in Engineering Monographs on Earthquake Criteria, Structural Design, and Strong Motion Records, v. 5, by H. B. Seed and I. M. Idriss (1982), Earthquake Engineering Research Institute.

Seed, H. B., Ugas, C., and Lysmer, J., 1976, Site-dependent spectra for earthquake-resistant design, Bulletin of the Seismological Society of America, v. 66, p. 221-224.

Trifunac, M. D., 1976, Preliminary empirical model for scaling Fourier amplitude spectra of strong motion acceleration in terms of earthquake magnitude, source-to-station distance and recording site condition, Bulletin of the Seismological Society of America, v. 66, p. 1343-1373.





QUESTION 17

Describe the analyses including the data bases used to determine the style of faulting factors derived from both the empirical and numerical studies.

There are both theoretical calculations and empirical data that suggest thrust faulting events may produce larger ground motions than strike-slip events. For example, ground motion simulation studies by Anderson and Luco (1983) indicate that sites located directly above the rupture surface of dipping faults had the highest amplitudes of any of the rupture configurations they tested. Boore and Boatwright (1984) found for a double-couple point source that the average radiation coefficients for dip-slip faulting were greater than for strike-slip faulting in the near field, and less than those for strike-slip faulting in the far field. They showed numerically that at distances within about a focal depth of the source, the ratio of average body wave radiation coefficient between thrust faulting and strike-slip faulting ranges from 1.14 to 1.28. Campbell (1981, 1987, 1988) has found differences in strong-motion amplitudes between strike-slip and thrust faulting events, with thrust faulting producing 18 to 46 percent higher peak accelerations than strike-slip events. Table Q17-1 summarizes these results and the results from both the empirical and numerical modeling studies of the Long Term Seismic Program.

Empirical Ground-Motion Studies

Strong-motion data from rock and soil recording sites for the magnitude 4.8 to 7.4 range were examined for evidence of differences in ground motion as a function of style of faulting. Figure Q17-1 shows our combined strong-motion rock and soil data for thrust and strike-slip events of magnitude 6.3 to 6.7, normalized to a common magnitude of 6.5. The figure clearly shows that on an overall basis, the peak ground acceleration values associated with thrust earthquakes are higher than those associated with the strike-slip earthquakes.

The significance of faulting type was tested for the combined rock and soil data using multiple regression. Figures Q17-2 and Q17-3 show the normalized residuals as functions of distance and magnitude, respectively. These residuals were obtained by using the following equation for the combined thrust and strike-slip rock and soil data:

$$\ln(a_{\max}) = C_1 + C_2M - C_3 \ln [R + C_4 \exp(C_5M)] \quad (1)$$

The results indicate a tendency for thrust faulting events to produce larger peak accelerations, as demonstrated by the mean value of the normalized residuals for thrust events being higher than that for strike-slip events. The statistical significance of the observed differences was checked by modifying equation (1) to include a "dummy" variable (Draper and Smith, 1981), Z_f , for style of faulting, yielding the relationship

$$\ln(a_{\max}) = C_1 + C_2M - C_3 \ln [R + C_4 \exp(C_5M)] + C_6Z_f \quad (2)$$

where Z_f takes on the value 0 for strike-slip faulting and 1 for thrust faulting. Fitting equation (2) to the combined rock and soil data for the magnitude 4.8 to 7.4 range yields a value of 0.24 ± 0.05 for parameter C_6 , corresponding to 27 percent higher peak accelerations for thrust faulting events compared with strike-slip events. The value of 0.24 for parameter C_6 corresponds to the difference between the mean value of the normalized residuals for thrust faulting events and the mean value for strike-slip faulting events shown in Figures Q17-2 and Q17-3.

A similar analysis of the combined rock and soil data for magnitude 6.3 or greater earthquakes yields a value of 0.2 ± 0.06 for parameter C_6 . The value of 0.2 corresponds to 22 percent higher accelerations for thrust faulting events compared with strike-slip events.



Table Q17-1

EFFECT OF STYLE OF FAULTING ON PEAK GROUND ACCELERATION

<u>Empirical Relationships</u>	<u>Ratio of PGA for Thrust Faulting to PGA for Strike-Slip Faulting</u>
Campbell (1981)	1.17 - 1.28
Campbell (1987)	1.38 - 1.40
Campbell (1988)	1.46
Long Term Seismic Program	
All magnitudes (M 4.8 to 7.4)	1.27
Magnitude 6.3 or greater	1.22
<u>Numerical Simulations</u>	
Boore and Boatwright (1984)	1.14 - 1.28
Long Term Seismic Program	1.16
<u>Selected for Long Term Seismic Program</u>	<u>1.2</u>



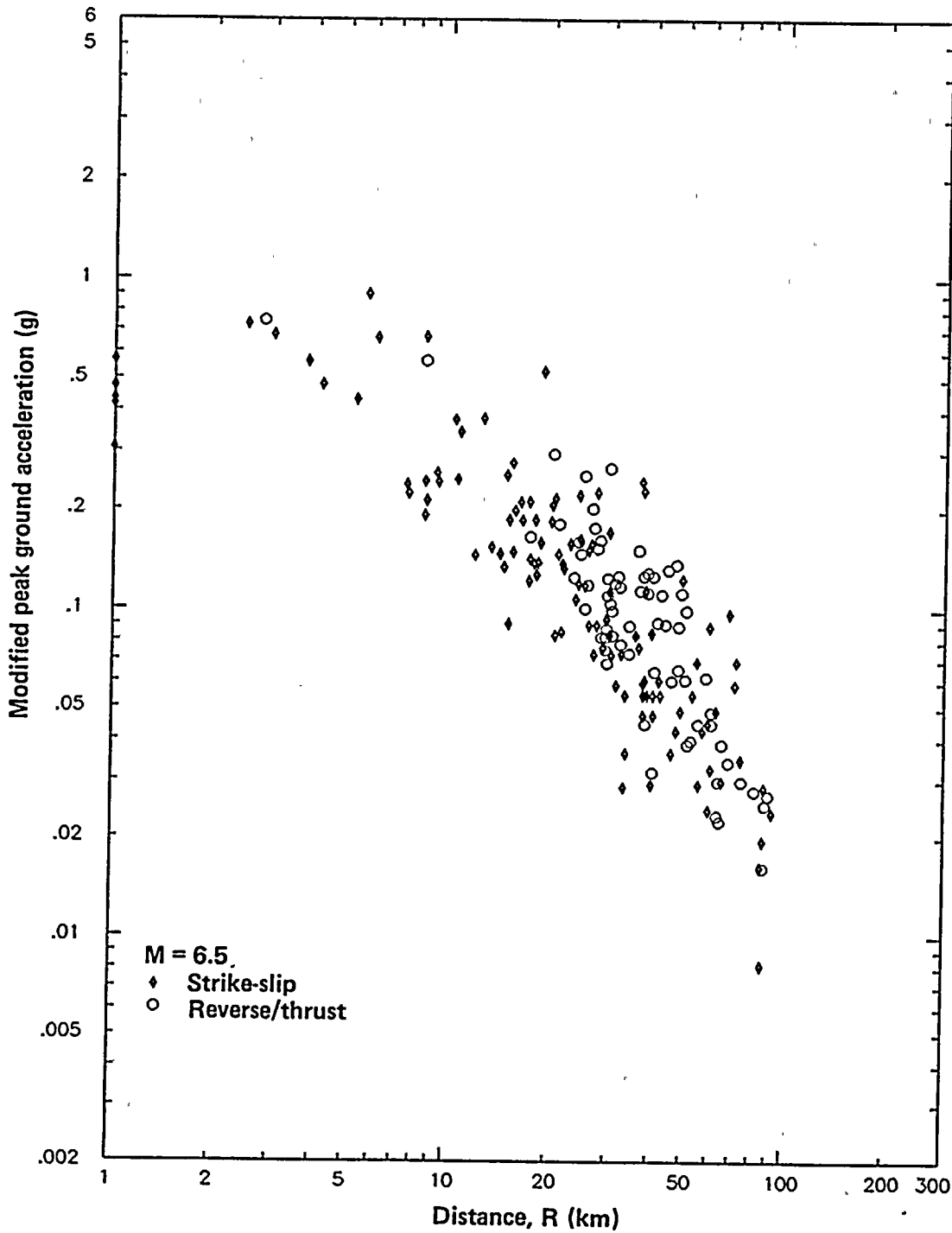


Figure Q17-1

Rock and soil data base for magnitude 6.3 to 6.7 earthquakes, normalized to magnitude 6.5 (within 10 km).



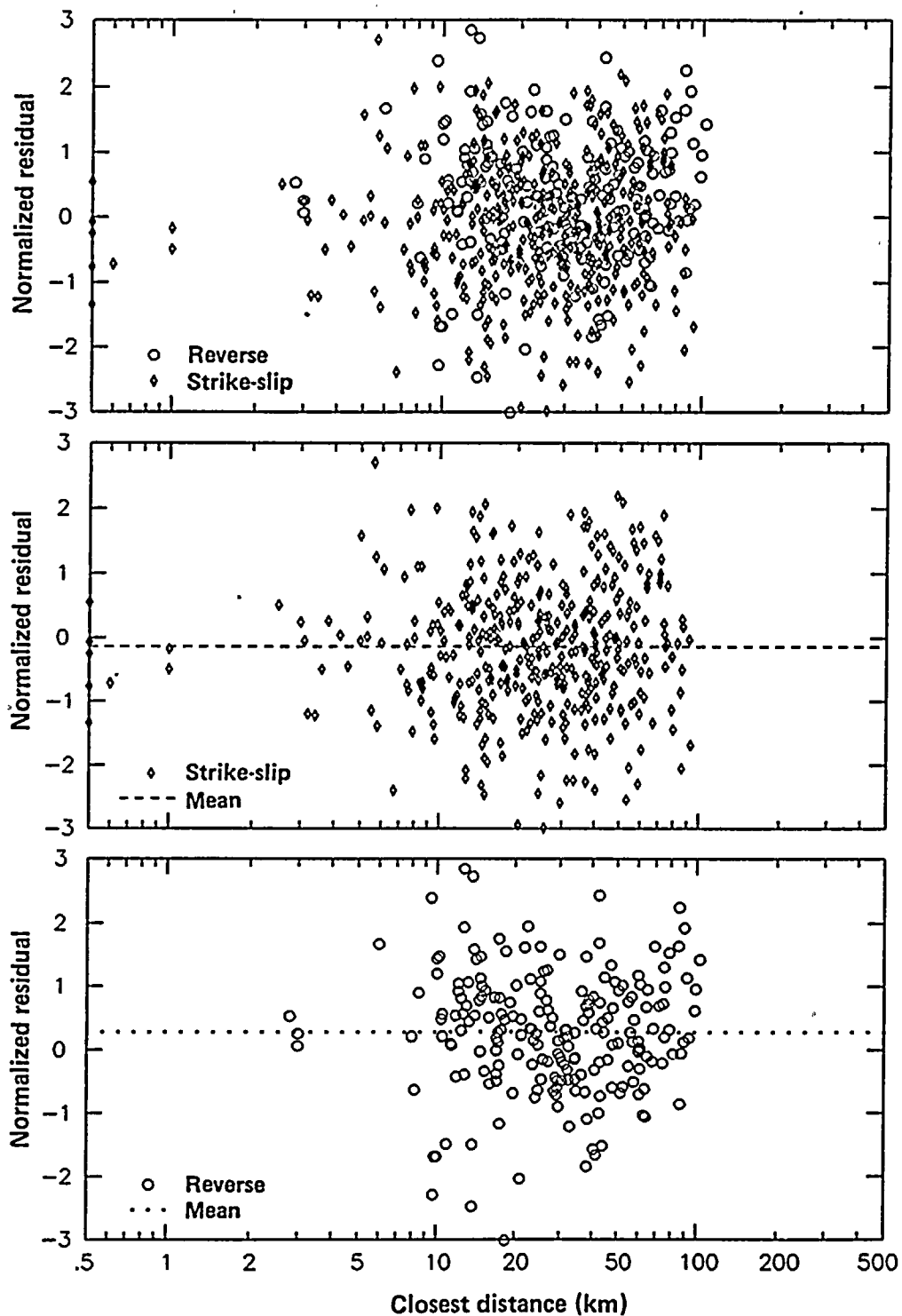


Figure Q17-2

Normalized residuals versus distance for Equation (1) using rock- and soil-site recordings.



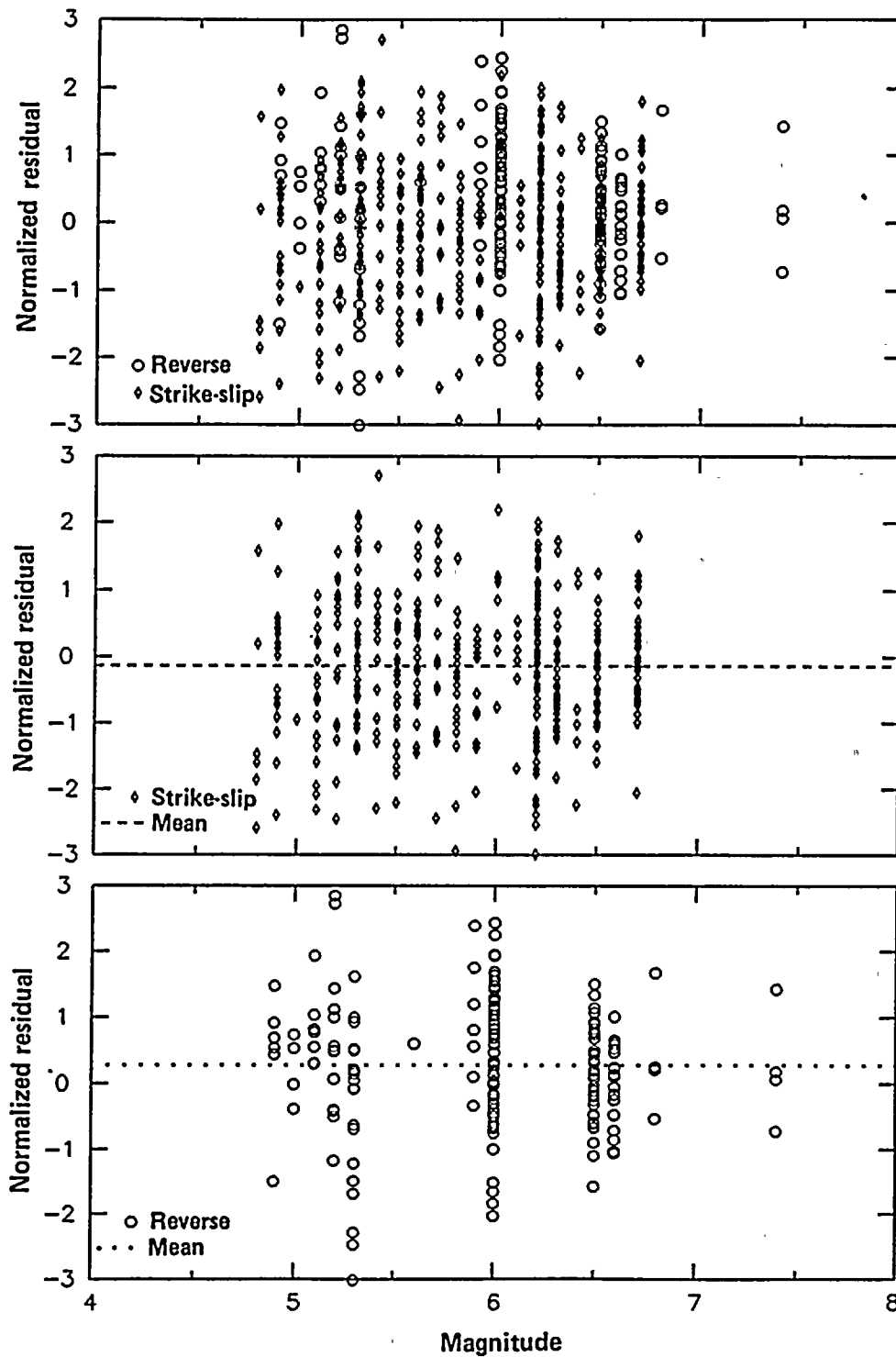


Figure Q17-3

Normalized residuals versus magnitude for Equation (1) using rock- and soil-site recordings.



Numerical Ground-Motion Studies

A suite of simulations was generated for moment magnitude 7.2 earthquakes having vertical strike-slip faulting, oblique faulting on a plane dipping at 60 degrees, and thrust faulting on a plane dipping at 35 degrees. The orientation of the fault models is shown in Figure Q17-4; the recording station is on the hanging-wall side of the oblique and thrust faults. The dimensions of the fault models and their discretization into fault elements are shown in Figure Q17-5, and the slip distributions are shown in Tables Q17-2 through Q17-4. Ground motions were simulated at stations parallel to the fault strike at the locations indicated in Figure Q17-5; eleven stations for the strike-slip fault, ten stations for the oblique fault, and eight stations for the thrust fault. Simulations for both bilateral and unilateral rupture were generated, yielding a total of 22 strike-slip simulations, 20 oblique simulations and 16 thrust simulations.

The average peak accelerations for the strike-slip, oblique, and thrust fault models are 0.351 g, 0.375 g, and 0.406 g, respectively. The peak accelerations for oblique and thrust faulting are 7 and 16 percent larger, respectively than for strike-slip faulting, as shown in Table Q17-5.

Table Q17-5

EFFECT OF FAULTING STYLE ON PEAK GROUND ACCELERATION (Based on numerical modeling studies)

<u>Faulting Style</u>	<u>PGA (g)</u>	<u>Relative to Strike-slip</u>
Strike-Slip	0.351	1.0
Oblique	0.375	1.07
Thrust	0.406	1.16

Selected Adjustment Factors for Style of Faulting

Quantification of the effect of style of faulting on ground motions was based on literature review, analysis of soil and rock data sets, and numerical modeling results (Tables Q17-1 and Q17-5). On the basis of these studies, the following relative scaling factors on peak ground acceleration and spectral acceleration for the style of faulting were used to convert the ground motions from thrust style of faulting to other styles of faulting.

<u>Style of Faulting</u>	<u>Scaling Factor</u>
Strike-slip	0.83
Oblique	0.91
Thrust	1.0

References

Anderson, J. G., and Luco, J. E., 1983, Parametric study of near-field ground motions for oblique-slip and dip-slip dislocation models, Bulletin of the Seismological Society of America, v. 73, p. 45-



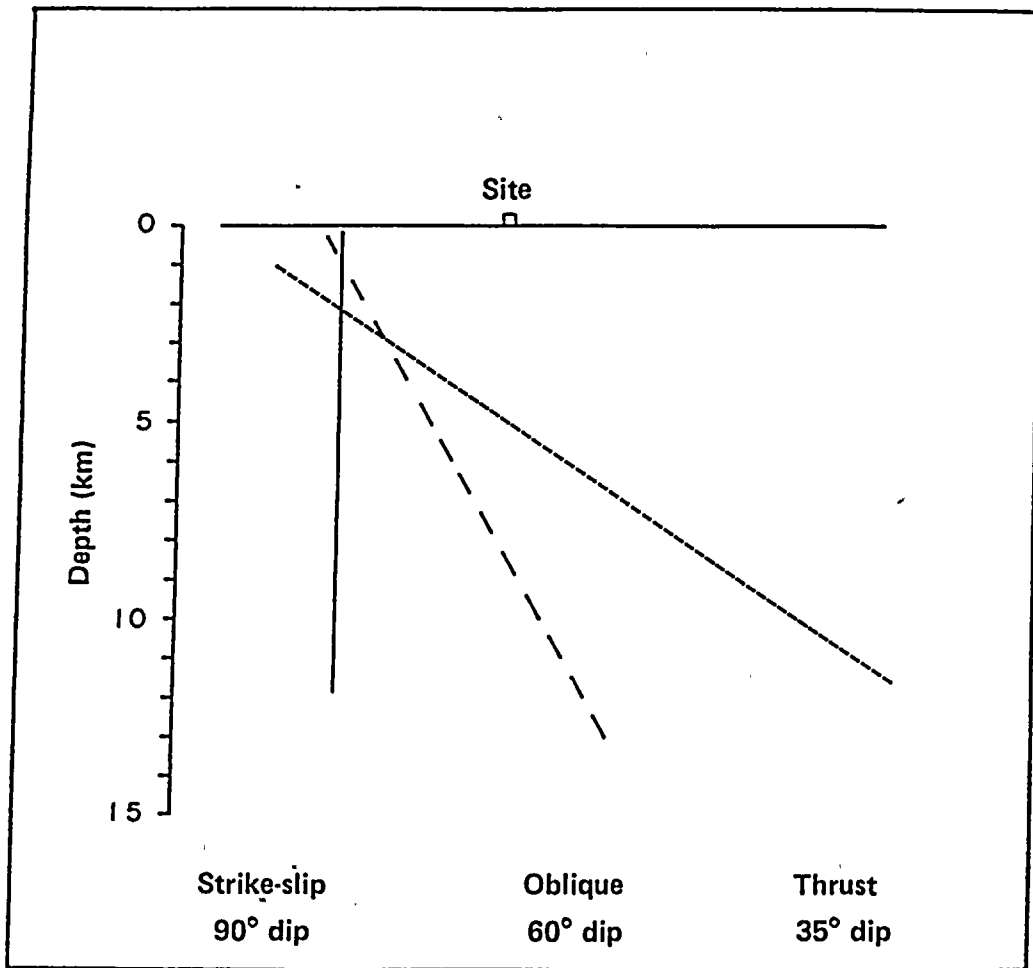


Figure Q17-4

Vertical cross section of fault models used to examine the effect of styling of faulting on simulated ground motions.



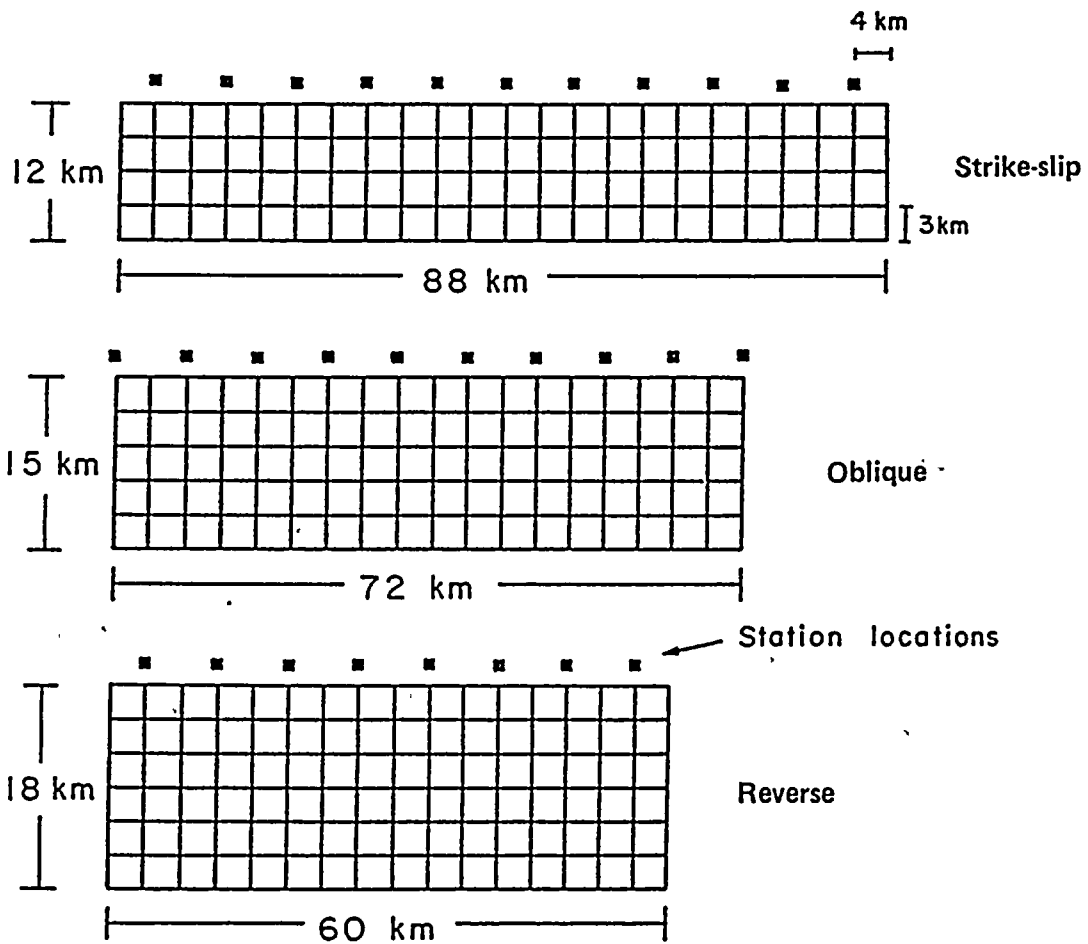


Figure Q17-5

Fault element geometry and station locations of fault models used to estimate style of faulting factors for numerical modeling.



Table Q17-2

SLIP (M) ON THE FAULT ELEMENTS OF THE STRIKE-SLIP MODEL

1.0	1.0	1.0	1.6	2.0	1.6	1.0	1.0	1.0	1.6	2.0	1.6	1.0	1.0	1.0	1.0	1.0	3.1	5.1	3.1	1.0	1.0
1.0	1.0	1.0	3.0	5.0	3.0	1.0	1.0	1.0	1.0	3.0	5.0	3.0	1.0	1.0	1.0	2.0	5.0	10.1	5.0	2.0	1.0
1.0	1.0	2.0	5.0	10.1	5.0	2.0	1.0	1.0	2.0	5.0	10.1	5.0	2.0	1.0	1.0	2.0	5.0	10.1	5.0	2.0	1.0
1.0	1.0	1.0	3.0	5.0	3.0	1.0	1.0	1.0	1.0	3.0	5.0	3.0	1.0	1.0	1.0	1.0	3.0	5.0	3.0	1.0	1.0

Table Q17-3

SLIP (M) ON THE FAULT ELEMENTS OF THE OBLIQUE MODEL

1.1	1.1	1.1	1.8	2.2	1.8	1.1	1.1	1.1	1.1	1.1	1.1	1.8	2.2	1.8	1.1	1.1	1.1	1.1
1.1	1.1	1.1	3.2	5.3	3.2	1.1	1.1	1.1	1.1	1.1	1.1	3.2	5.3	3.2	1.1	1.1	1.1	1.1
1.1	1.1	2.1	5.3	10.6	5.3	2.1	1.1	1.1	1.1	2.1	5.3	10.6	5.3	2.1	1.1	1.1	1.1	1.1
1.1	1.1	2.1	5.3	10.6	5.3	2.1	1.1	1.1	1.1	2.1	5.3	10.6	5.3	2.1	1.1	1.1	1.1	1.1
1.0	1.0	1.0	2.9	4.8	2.9	1.0	1.0	1.0	1.0	1.0	2.9	4.8	2.9	1.0	1.0	1.0	1.0	1.0

Table Q17-4

SLIP (M) ON THE FAULT ELEMENTS OF THE THRUST MODEL

1.0	1.0	1.0	1.0	2.0	1.0	1.0	1.0	1.0	1.0	1.0	2.0	1.0	1.0	1.0	1.0
1.0	1.0	1.0	2.0	4.0	2.0	1.0	1.0	1.0	1.0	2.0	4.0	2.0	1.0	1.0	1.0
1.0	1.0	2.0	4.0	7.0	4.0	2.0	1.0	1.0	2.0	4.0	7.0	4.0	2.0	1.0	1.0
1.0	1.0	3.0	7.0	10.0	7.0	3.0	1.0	1.0	3.0	7.0	10.0	7.0	3.0	1.0	1.0
1.0	1.0	2.0	4.0	7.0	4.0	2.0	1.0	1.0	2.0	4.0	7.0	4.0	2.0	1.0	1.0
1.0	1.0	1.0	2.0	4.0	2.0	1.0	1.0	1.0	1.0	2.0	4.0	2.0	1.0	1.0	1.0



Core, D. M., and Boatwright, J. A., 1984, Average body-wave radiation coefficients, Bulletin of the Seismological Society of America, v. 74, p. 1615-1621.

Campbell, K. W., 1981, Near-source attenuation of peak horizontal acceleration, Bulletin of the Seismological Society of America, v. 71, no. 7, p. 2039-2070.

Campbell, K. W., 1987, Predicting strong ground motion in Utah, in Assessment of Regional Earthquake Hazards and Risk along the Wasatch Front, Utah, v. 2, U.S. Geological Survey Open File Report 87-585, p. L1-L90.

Campbell, K. W., 1988, Preliminary report on empirical studies of horizontal strong ground motion for the Diablo Canyon site, California, Report to the U.S. Nuclear Regulatory Commission, October, 1988.

Draper, N. R., and Smith, H., 1981, Applied regression analysis, second edition, New York, John Wiley and Sons.





QUESTION 18


It has been suggested that stress drops are higher for oblique and thrust faults than for strike-slip faults. What is the justification for using a constant stress drop of 50 bars for all fault types in the numerical modeling studies? To what extent would the use of higher stress drops impact the results?

From a review of published summaries of earthquake stress drops, we have found no evidence for dependence of stress drop on faulting style. In our review, we maintained the distinction between the "global stress drop," which represents the average stress drop over the fault plane, and the "local stress drop," which may vary with position on the fault plane.

Global Static Stress Drop

The global static stress drop is derived from the static fault parameters of the earthquake. To the extent that some part of the faulting process may occur aseismically or in a series of multiple events, this measure of stress drop is not directly related to the wave field radiated by the earthquake, and therefore may not necessarily be reflected in strong ground motion amplitudes, particularly at high frequencies.

Kanamori and Anderson (1975) compiled the observed seismic moment and fault rupture area for 41 interplate earthquakes (including transform and subduction events) and intraplate earthquakes (including events such as the 1952 Kern County and the 1971 San Fernando events, which occurred near but not on the plate interface). Both categories of earthquakes included a mixture of different types of faulting. There was no clear dependence of stress drop on faulting type.



Sykes and Quittmeyer (1981) estimated the static stress drop of 26 large interplate earthquakes using a rectangular dislocation model. Fourteen of these were strike-slip earthquakes, and twelve were thrust earthquakes. Again, there was no clear difference in the static stress drop between these two types of faulting. Both these studies also showed that the global stress drops for a large majority of large interplate earthquakes are smaller than 50 bars.

Global Rupture Duration Stress Drop

Another estimate of global stress drop can be derived from rupture duration, which provides a direct measure of the average rate of release of seismic moment during an earthquake. This measure of stress drop differs from the static stress drops discussed above, and is expected to be more directly reflected in ground-motion amplitudes.

The global stress drops based on rupture duration for crustal earthquakes in western North America were derived by Somerville and others (1987). Their data set included all types of fault mechanisms. The results of that study also do not support the suggestion that thrust or oblique mechanisms produce larger stress-drops.

Local Stress Drop

The global stress drop values described above pertain to a model in which stress is released uniformly over a fault surface. However, in our simulation procedure, the slip on the fault plane is heterogeneous, giving rise to a spatially variable "local stress drop," whose value is controlled by the dimensions and amount of slip on asperities. The amplitudes of high frequency ground motions close to an earthquake are expected to reflect this local stress drop, rather than the average stress drop over the fault. However, for an earthquake characterized by seismic moment release on one main asperity, the seismic radiation may only be discernible during the rupture of this asperity, and the source duration stress drop that is estimated may be comparable to the local stress drop.



our simulations at the site, the asperities have maximum slip values of about 10 meters and dimensions of about 12 x 12 km, corresponding to local stress drops of approximately 500 bars. These values are larger than the largest local stress drops that have been reported from moderate and large earthquakes in California. For example, Papageorgiou and Aki (1983), using a specific barrier model, estimated local stress drops in the range of 200 to 370 bars for seven moderate to large California earthquakes. Among these seven events, there does not appear to be a systematic difference in local stress drop between the two events having reverse/oblique mechanisms and the five events having strike-slip mechanisms. The source models used in our site simulations already have local stress drops larger than any that have been observed in large earthquakes in California; it is not appropriate to consider larger local stress drops.

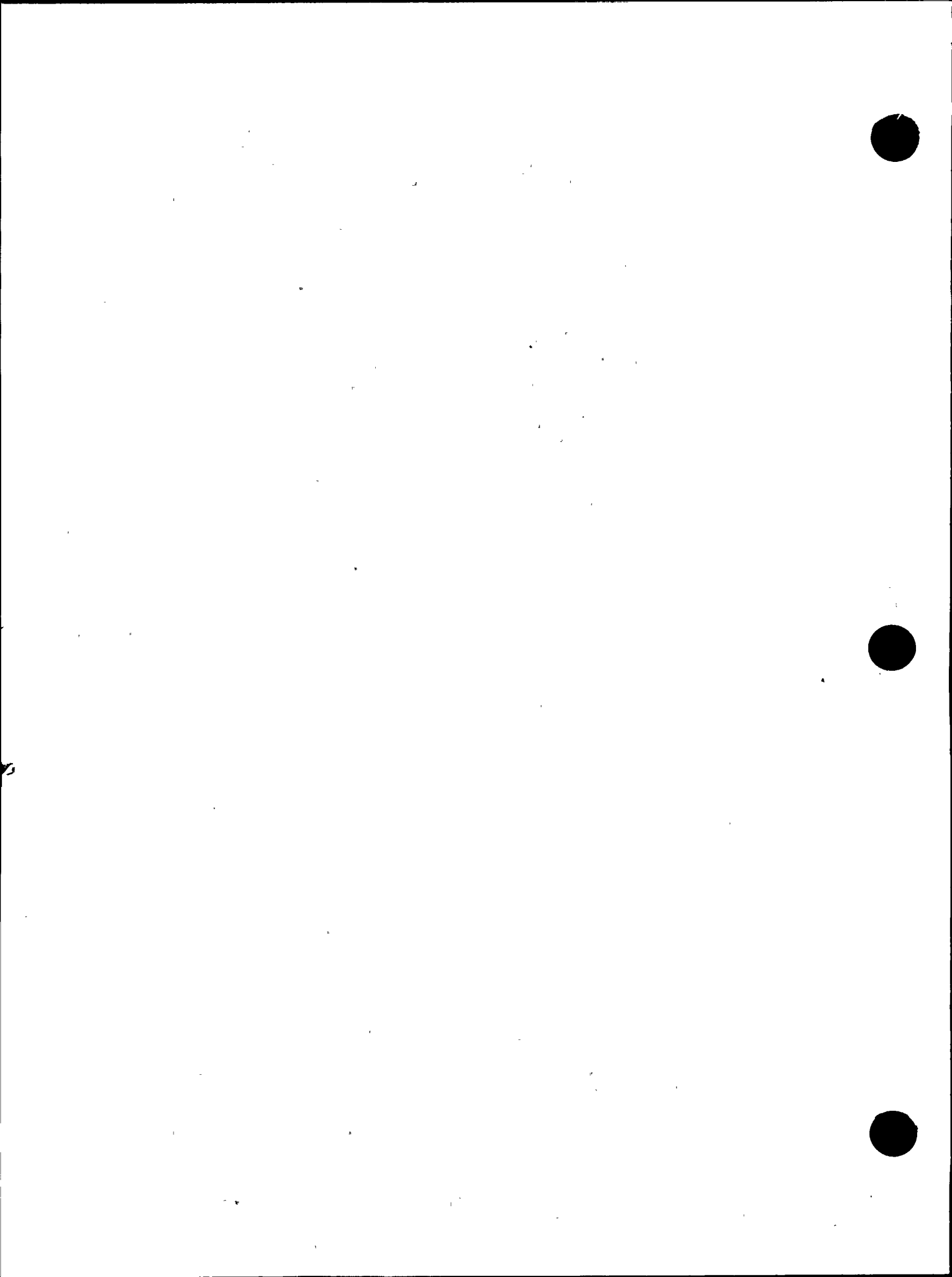
Conclusion

From a review of published summaries of earthquake stress drops, we have found no evidence for dependence of stress drop on faulting style. The global stress drop of 50 bars that was used for all fault styles is a reasonable representation of the average global stress drop of California earthquakes. The local stress drops of 500 bars contained in the fault models, reflecting asperities with large displacements, are larger than any reported for California earthquakes. We, therefore, conclude that it is not appropriate to consider larger stress drop values. Using larger global stress drops would result, on the average, in higher ground motions; however, the actual impact would also depend on the variation of local stress drop across the fault plane.

References

- Kanamori, H., and Anderson, D. L., 1975, Theoretical basis of some empirical relations in seismology, *Bulletin of the Seismological Society of America*, v. 65, p. 1073-1095.
- Papageorgiou, A. S., and Aki, K., 1983, A specific barrier model for the quantitative description of inhomogeneous faulting and the prediction of strong ground motion. Part II. Applications of the model. *Bulletin of the Seismological Society of America*, v. 73, p. 953-978.
- Somerville, P. G., McLaren, J. P., LeFevre, L. V., Burger, R. W., and Helmberger, D. V., 1987, Comparison of source scaling relations of eastern and western North American earthquakes, *Bulletin of the Seismological Society of America*, v. 77, p. 322-346.
- Sykes, L. R., and Quittmeyer, R. C., 1981, Repeat times of great earthquakes along simple plate boundaries, in *Earthquake Prediction - an International Review*, Maurice Ewing series 4, edited by D. W. Simpson and P. G. Richards, American Geophysical Union, Washington, D.C., p. 217-247.





 QUESTION 19

Directivity effects have been observed from earthquake ruptures propagating toward and away from seismic stations. There do not appear to be any directivity effects observed in the ground motions from the numerical modeling studies; although, from the geometry of the station array they might be expected. Is this an artifact of the way the simulations are performed?

The directivity effects that have been observed in recorded strong motion data are generally more pronounced at low frequencies (less than about 5 Hz) than at high frequencies (above about 5 Hz). Although directivity effects have been observed in some peak accelerations (such as for the magnitude 5.8 and 5.5 Livermore earthquakes of January, 1980 (Boatwright and Boore (1982)), directivity effects are not generally seen in peak accelerations. However, they are often observed in strong ground motions at lower frequencies, as was the case for the magnitude 6.6 San Fernando earthquake of February 9, 1971 (Heaton and Helmberger, 1979), the magnitude 6.2 Morgan Hill earthquake of April 24, 1984 (Niazi, 1984), and the magnitude 6.5 October 15, 1979 Imperial Valley earthquake (Singh, 1981; Niazi, 1982). Bolt (1983) concluded that definitive evidence for directivity effects at high frequencies is limited and somewhat contradictory. He inferred that the directivity effect is probably greatest for ground displacements and velocities, and least for peak accelerations; he postulated that high-frequency ground motions have variations due to scattering, attenuation, and source asperities that mask directivity effects.

In our response to Question 17a, January 1989, we showed the distribution of averaged horizontal peak acceleration along a strike-slip model of the Hosgri fault for unilateral rupture propagation (Figure Q19-1). The fault model was similar to that used in generating estimates of the site-specific response spectrum, except that the spatial distribution of slip was made uniform to isolate directivity effects from effects due to variations in slip. We concluded that the effect of directivity on the averaged horizontal peak acceleration is not significant.

We have done additional simulations for vertical strike-slip faults to further investigate directivity effects. We considered both unilateral and bilateral rupture modes, and the slip distribution on the fault was again kept uniform to highlight the directivity effect. Simulations were performed using four different sets of random numbers; these random numbers provide a stochastic component to otherwise uniform rupture velocity and slip velocity, as described in our response to Question 12, January 1989.

For stations located at a fixed normal distance from the fault rupture surface, the directivity effect would produce peak motions that increase with distance away from the epicenter. For some random number sets, directivity effects are observed in peak acceleration (Figure Q19-2), but in other cases they are not. When the results of four simulations that use different sets of random numbers are averaged, the directivity effect is not apparent in the peak accelerations. This is seen in the top parts of Figures Q19-3 and Q19-4, which show the averaged peak acceleration as a function of position along the fault for unilateral and bilateral rupture modes, respectively.

The fact that the fault-normal component is consistently larger than the fault-parallel component is due to radiation pattern effects. For a vertical strike-slip fault, the peak accelerations are expected to be largest on the fault-normal component, because this component consists mostly of SH waves near a radiation pattern maximum for all but the closest fault element contributions. The fault-parallel component consists mostly of nearly nodal SV waves for all but the closest fault element contributions, and is thus expected to be smaller. Our results are consistent with these expectations.

At lower frequencies, directivity effects are seen for each of the four random number sets used in the simulations. The lower parts of Figures Q19-3 and Q19-4 show the distribution along the fault of peak displacements, averaged over the four random number sets and normalized by the values of the fault-parallel component at station 40. For both unilateral and bilateral rupture, the peak amplitudes of the fault-normal component tend to increase away from the epicenter, consistent with the expected





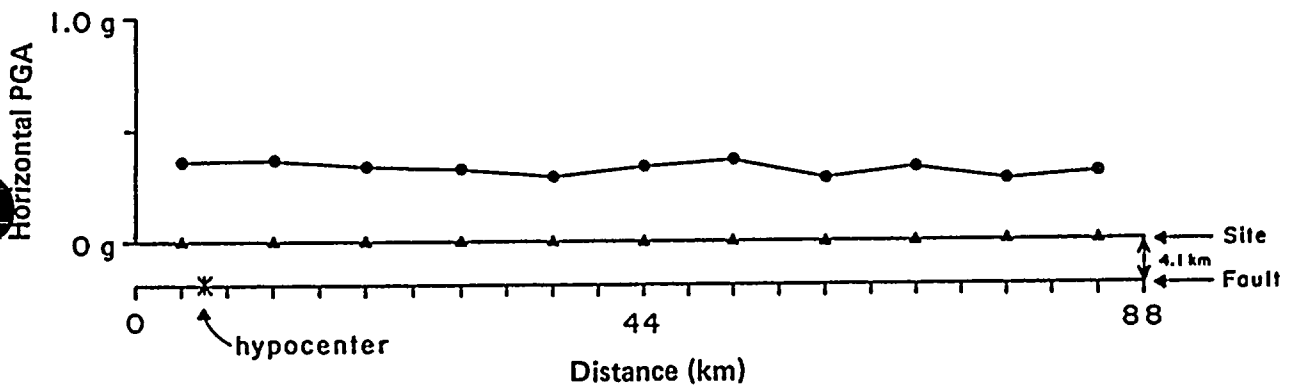


Figure Q19-1

Illustration of the directivity effect for a unilateral strike-slip rupture on the Hosgri fault. The rupture segment and the line of stations parallel to the fault zone are shown in map view below. The variation of the average peak ground acceleration of the two horizontal components, along the line of stations, is shown above.



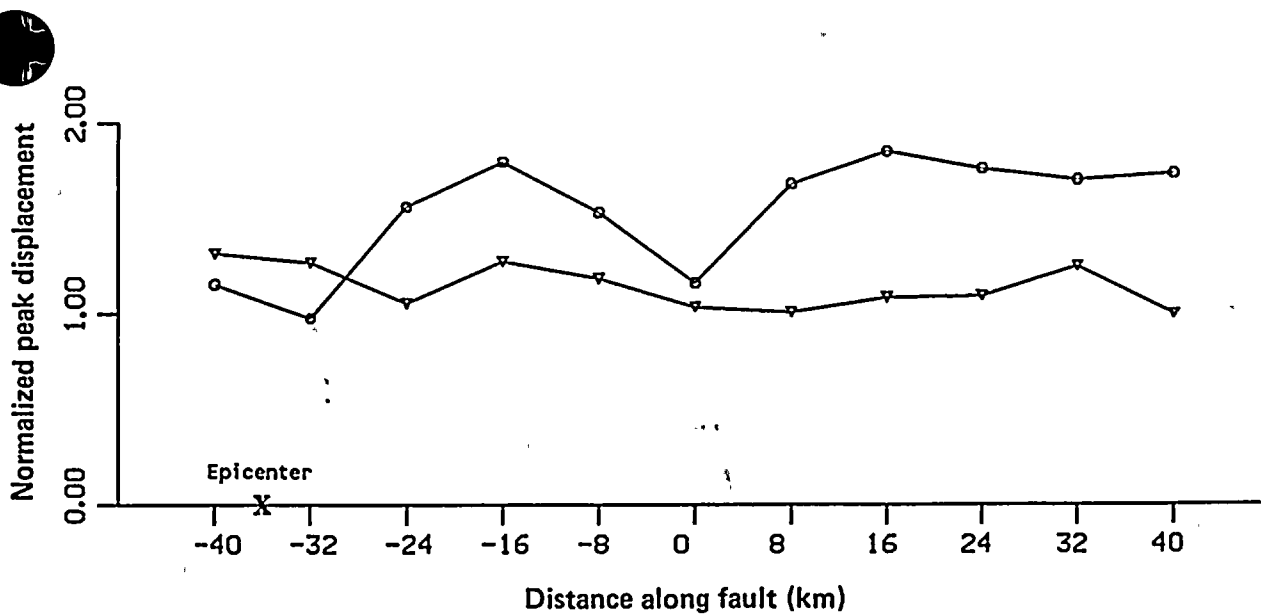
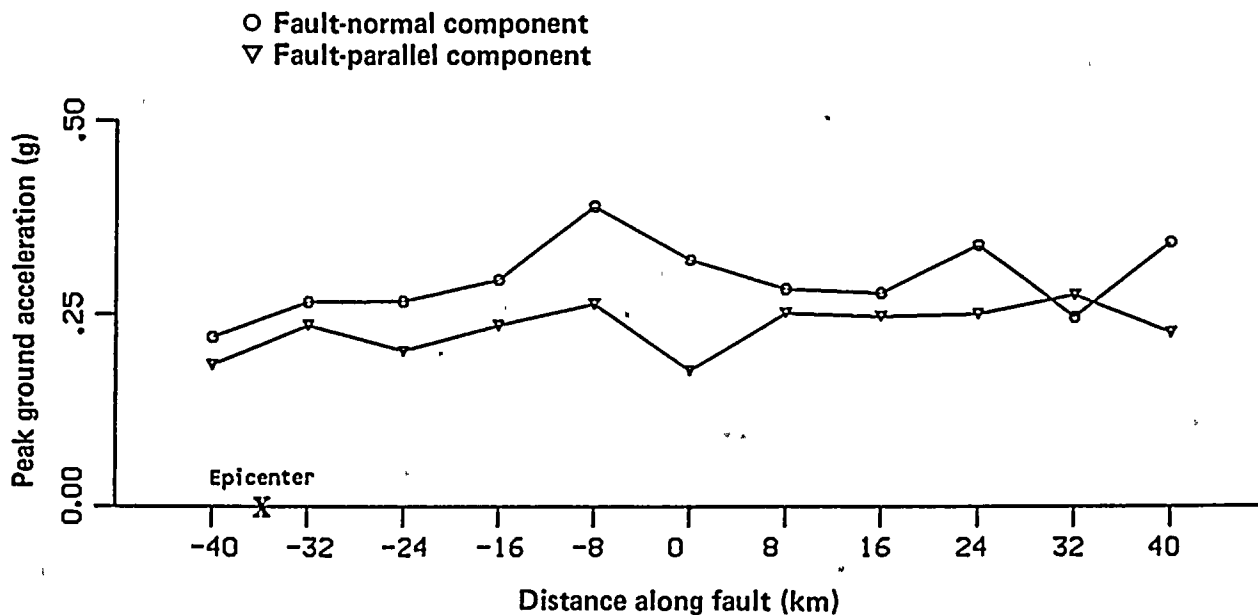


Figure Q19-2

Distribution of peak acceleration (above) and normalized peak displacement (below) along a laterally propagating strike-slip fault for one particular realization of simulations.



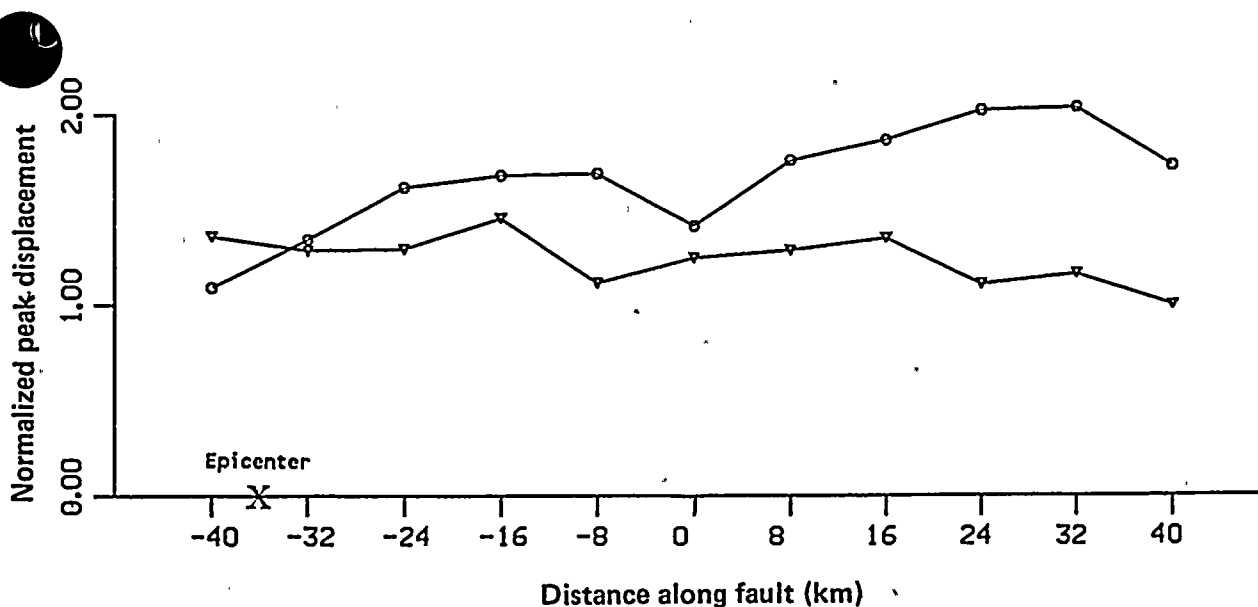
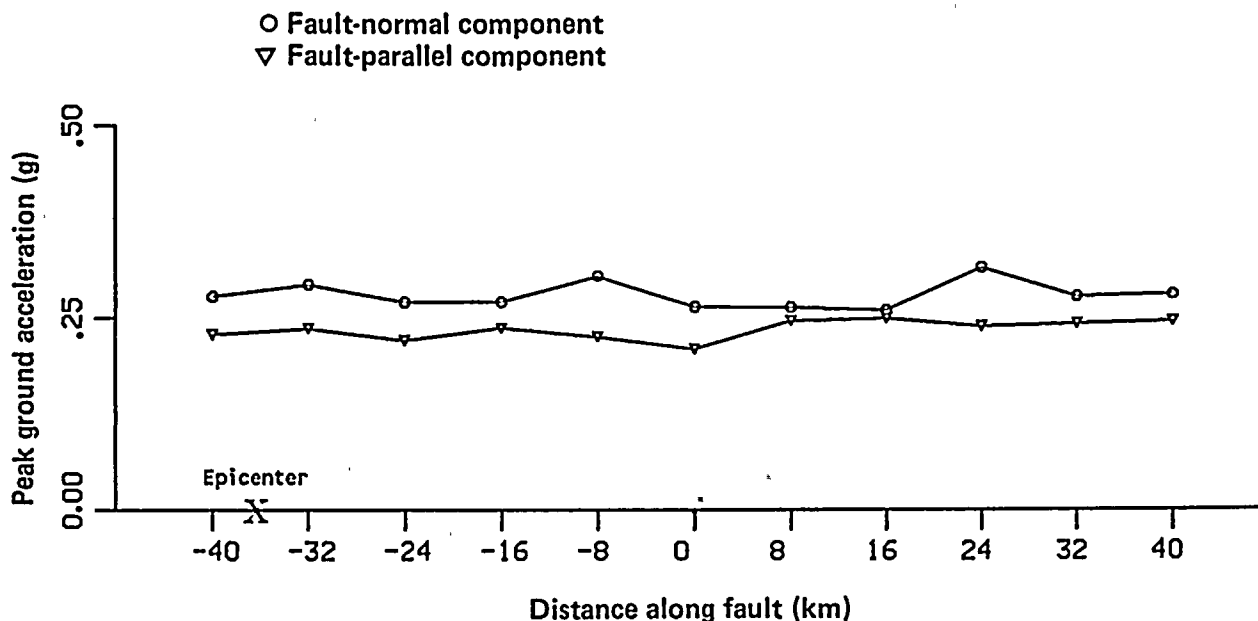


Figure Q19-3

Distribution of peak acceleration (above) and normalized peak displacement (below) along a laterally propagating strike-slip fault, averaged over four simulations.



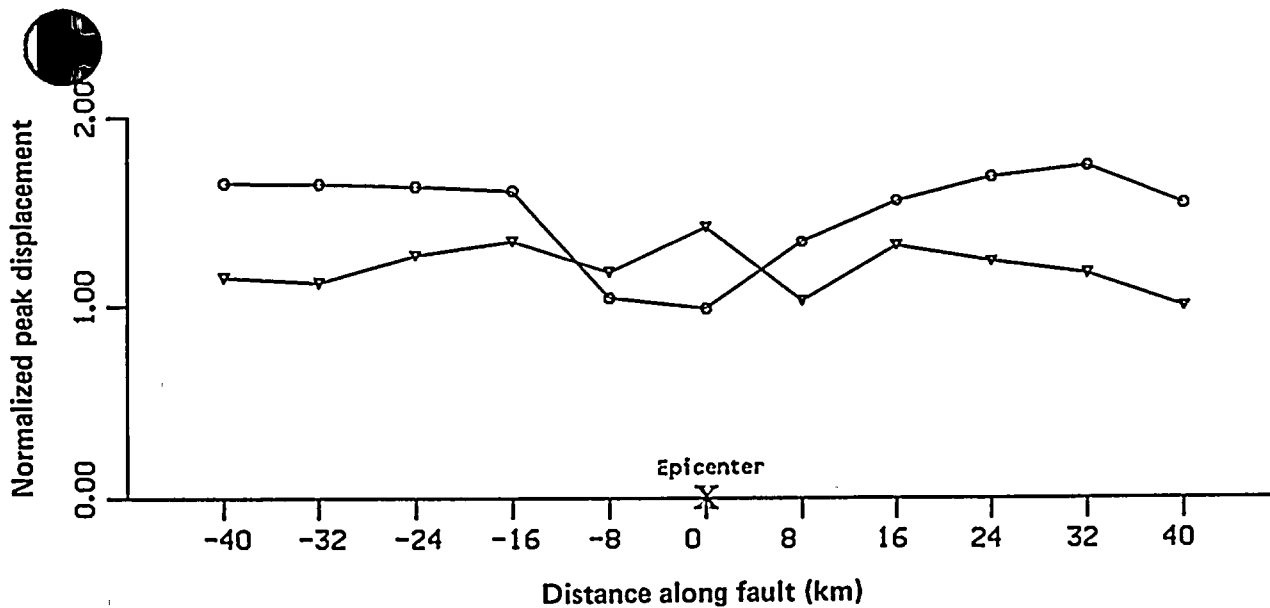
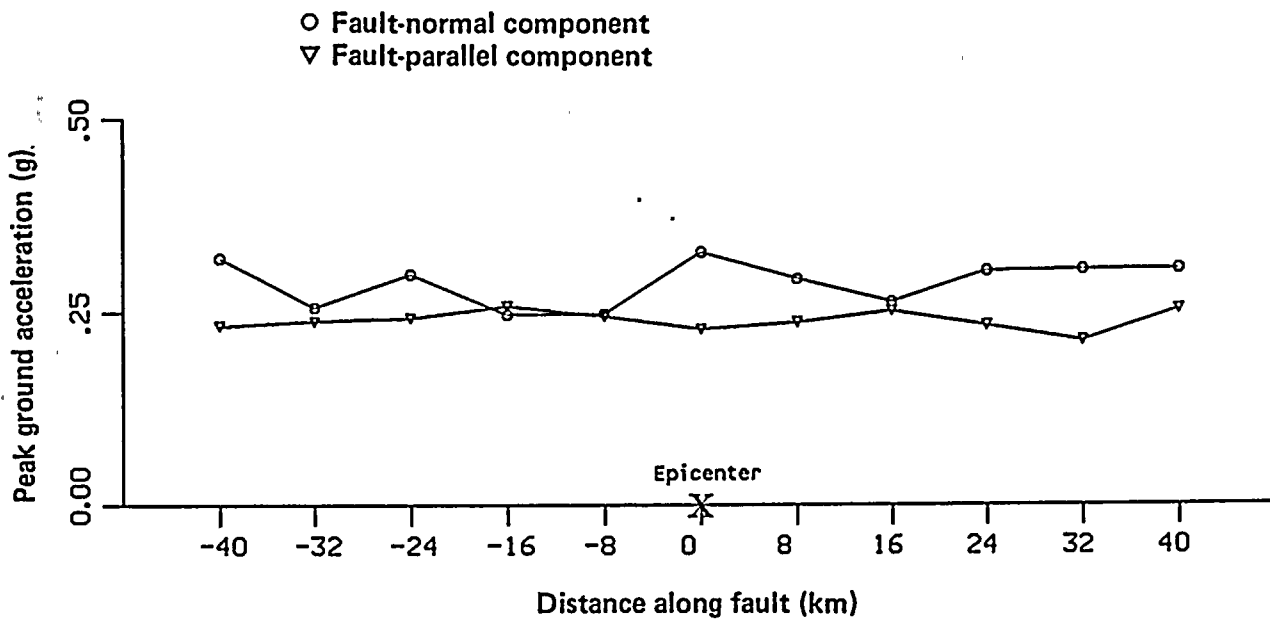


Figure Q19-4

Distribution of peak acceleration (above) and normalized peak displacement (below) along a bilaterally propagating strike-slip fault, averaged over four simulations.



Directivity effect. However, the fault-parallel component does not show a directivity effect. The presence of the directivity effect on the SH-rich fault-normal component but not on the SV-rich fault-parallel component may be due to the fact that the SV waves along the fault are nodal but the SH waves are near their radiation pattern maximum.

Conclusion

We conclude that the simulation procedure does give rise to directivity effects. These effects are always present at lower frequencies, are not always present at higher frequencies, and are generally not significant at the high frequencies that control peak acceleration. These characteristics of the directivity effect in the simulations are similar to those observed in strong motion recordings.

References

Boatwright, J., and Boore, D. M., 1982, Analysis of the ground motion accelerations radiated by the 1980 Livermore Valley earthquakes for directivity and dynamic source characteristics: *Bulletin of the Seismological Society of America*, v. 72, p. 1843-1865.

Bolt, B. A., 1983, The contribution of directivity focusing to earthquake intensities: Report 20, State-of-the-art for Assessing Earthquake Hazards in the United States, Miscellaneous Paper s-73-1, U.S. Army Engineer Waterways Experiment Station, Vicksburg, Miss.

Heaton, T. H., and Helmberger, D. V., 1979, Generalized ray models of the San Fernando earthquake: *Bulletin of the Seismological Society of America*, v. 69, p. 1311-1341.

Niazi, M., 1982, Source dynamics of the 1979 Imperial Valley earthquake from near-source observations (of ground motion acceleration and velocity): *Bulletin of the Seismological Society of America*, v. 72, p. 1957-1968.

Niazi, M., 1984, Radial asymmetry of the observed PGA and question of focusing in the near source region of April 24, 1984 Morgan Hill earthquake; in *The 1984 Morgan Hill Earthquake: California Division of Mines and Geology Special Publication 68*, p. 265-271.

Singh, J. P., 1981, The influence of source directivity on strong ground motions: Ph.D. Dissertation, University of California, Berkeley.



